Astronomy
&
Astrophysics

CALIFA, the Calar Alto Legacy Integral Field Area survey

IV. Third public data release[*,**]

S. F. Sánchez[1], R. García-Benito[2], S. Zibetti[3], C. J. Walcher[4], B. Husemann[5], M. A. Mendoza[2], L. Galbany[6,7],
J. Falcón-Barroso[8,10], D. Mast[11,12], J. Aceituno[13], J. A. L. Aguerri[8], J. Alves[9], A. L. Amorim[14], Y. Ascasibar[20],
D. Barrado-Navascues[13,15], J. Barrera-Ballesteros[16], S. Bekeraitè[4], J. Bland-Hawthorn[17], M. Cano Díaz[1],
R. Cid Fernandes[14], O. Cavichia[18], C. Cortijo[2], H. Dannerbauer[8], M. Demleitner[19], A. Díaz[20], R. J. Dettmar[21],
A. de Lorenzo-Cáceres[22,23], A. del Olmo[2], A. Galazzi[3], B. García-Lorenzo[8], A. Gil de Paz[24], R. González Delgado[2],
L. Holmes[25], J. Iglésias-Páramo[2], C. Kehrig[2], A. Kelz[4], R. C. Kennicutt[26], B. Kleemann[21], E. A. D. Lacerda[14],
R. López Fernández[2], A. R. López Sánchez[17], M. Lyubenova[27], R. Marino[28], I. Márquez[2], J. Mendez-Abreu[22],
M. Mollá[29], A. Monreal-Ibero[30], R. Ortega Minakata[31], J. P. Torres-Papaqui[32], E. Pérez[2], F. F. Rosales-Ortega[33],
M. M. Roth[4], P. Sánchez-Blázquez[20,34], U. Schilling[21], K. Spekkens[25], N. Vale Asari[14], R. C. E. van den Bosch[35],
G. van de Ven[35], J. M. Vilchez[2], V. Wild[22], L. Wisotzki[4], A. Yıldırım[35], and B. Ziegler[9]

(Affiliations can be found after the references)

ABSTRACT

This paper describes the third public data release (DR3) of the Calar Alto Legacy Integral Field Area (CALIFA) survey. Science-grade quality data for 667 galaxies are made public, including the 200 galaxies of the second public data release (DR2). Data were obtained with the integral-field spectrograph PMAS/PPak mounted on the 3.5 m telescope at the Calar Alto Observatory. Three different spectral setups are available: i) a low-resolution V500 setup covering the wavelength range 3745–7500 Å (4240–7140 Å unvignetted) with a spectral resolution of 6.0 Å (FWHM) for 646 galaxies, ii) a medium-resolution V1200 setup covering the wavelength range 3650–4840 Å (3650–4620 Å unvignetted) with a spectral resolution of 2.3 Å (FWHM) for 484 galaxies, and iii) the combination of the cubes from both setups (called COMBO) with a spectral resolution of 6.0 Å and a wavelength range between 3700–7500 Å (3700–7140 Å unvignetted) for 446 galaxies. The Main Sample, selected and observed according to the CALIFA survey strategy covers a redshift range between 0.005 and 0.03, spans the color-magnitude diagram and probes a wide range of stellar masses, ionization conditions, and morphological types. The Extension Sample covers several types of galaxies that are rare in the overall galaxy population and are therefore not numerous or absent in the CALIFA Main Sample. All the cubes in the data release were processed using the latest pipeline, which includes improved versions of the calibration frames and an even further improved image reconstruction quality. In total, the third data release contains 1576 datacubes, including ~1.5 million independent spectra.

Key words. galaxies: evolution – galaxies: general – techniques: spectroscopic – surveys

1. Introduction

The advent of large imaging surveys, complemented in some cases by single-fiber spectroscopy (e.g., Sloan Digital Sky Survey, SDSS; Galaxy and Mass Assembly survey, GAMA, York et al. 2000; Driver et al. 2009), has opened important new avenues for our understanding of galaxy evolution. However, one of the most significant limitations of these surveys is that they do not provide resolved spectroscopic information. Galaxies have long been known to be spatially extended objects, with observed properties that vary across their optical extents (e.g., Hubble 1926, 1936). Many of these properties vary coherently as a function of position relative to the galaxy center, and radial gradients have been studied for decades (e.g., Pagel & Edmunds 1981; Peletier 1989). Characterizing galaxies by assigning global values therefore oversimplifies their true complexity, and determining the spatially resolved properties of galaxies is fundamental to understanding the evolutionary processes that have shaped them. At the same time, evidence for a diversity in galaxy evolutionary histories as a function of mass and environment implies that statistically significant samples over large fractions of the sky are needed to understand the underlying physical mechanisms at work.

Thus, the logical next step for pushing beyond multiband imaging surveys (that provide detailed spatial information and limited spectral information) or single-aperture spectroscopic surveys (that sample only limited galaxy regions) is an Integral Field Spectroscopy (IFS) survey over a representative and statistically significant sample of galaxies. With this aim we undertook the Calar Alto Legacy Integral Field Area (CALIFA) survey in 2010 (Sánchez et al. 2012a) to obtain spatially resolved spectra for ~600 galaxies in the local Universe.

CALIFA was the first survey using imaging spectroscopy that was designed to provide a public dataset of a sample of galaxies representative of the Local Universe, i.e., this survey was foreseen to be a legacy survey from the outset. CALIFA thus aimed at extending the pioneering Spectrographic

---

[*] Based on observations collected at the Centro Astronómico Hispano Alemán (CAHA) at Calar Alto, operated jointly by the Max-Planck-Institut für Astronomie (MPIA) and the Instituto de Astrofísica de Andalucía (CSIC).

[**] The spectra are available at http://califa.caha.es/DR3

Areal Unit for Research on Optical Nebulae (SAURON) and Atlas3D surveys (Cappellari et al. 2011) to all galaxy types and larger wavelength coverage. The next generation of IFS surveys are already in progress – Mapping Nearby Galaxies at Apache Point Observatory survey (MaNGA, Bundy et al. 2015) and Sydney Australian-Astronomical-Observatory Multi-object Integral-Field-Spectrograph survey(SAMI, Croom et al. 2012). It is beyond the scope of this article to make a detailed comparison between these surveys and CALIFA, a topic that has already been addressed in previous articles (e.g., Sánchez 2015). Briefly, we note that MaNGA and SAMI will supplant all previous surveys in terms of number of objects. They have adopted a multiplexing scheme that allows us to observe several objects simultaneously. This increases the efficiency of collecting data in terms of number of objects, which was their main goal (10 000 objects, for MaNGA, and 3600 objects, for SAMI). CALIFA and Atlas3D use a single-IFU mode, which limits the number of objects to be observed simultaneously. On the other hand, the CALIFA and Atlas3D surveys observe a larger number of spectra per object, and offer better physical spatial sampling. One obvious manifestation of this is the very similar total number of spectra obtained by CALIFA, MaNGA, and SAMI, compared to the very different total number of objects to be observed.

The sample selections are also quite different. The MaNGA and SAMI samples cover a wider range of redshifts, from $z \sim 0.001$ to $z \sim 0.16$. Because the full width at half maximum (FWHM) of the point spread function (PSF) is very similar in the three surveys this implies a wide range of physical resolutions. Galaxies are thus sampled over a wider range of masses, but at different cosmological distances. On the contrary, the redshift range of the CALIFA and Atlas3D samples are rather small (Cappellari et al. 2011; Walcher et al. 2014), and therefore they present a better and more uniform physical sampling, making them optimal to study spatially resolved structures in galaxies (at ~1 kpc resolution).

Another important difference is the coverage of the different IFU surveys in terms of the optical extension of the galaxies. CALIFA observations cover most of the optical extension (beyond ~2.5 r_e) by construction, while Atlas3D reaches between 1–1.5 r_e on average. MaNGA comprises two main samples, where the goal is to reach either 1.5r_e (~70% of the targets) or 2.5r_e (~20%), and it hardly samples the outer regions for most of the galaxies (Ibarra-Mendel et al. 2016). Finally, SAMI, with the smallest FoV of all IFU surveys (16″/D) covers around ~1r_e of the galaxies (Bryant et al. 2015).

In summary the data provided by the CALIFA DR3 presented here occupy a niche which ensures high spatial resolution and good spatial coverage simultaneously, however, at the price of a smaller sample in comparison with currently ongoing surveys like MaNGA and SAMI. The CALIFA collaboration has addressed many different science cases using the information provided by these data, all of them focused on understanding the main properties of galaxies in the local Universe and the evolutionary processes that have shaped them: i) new techniques have been developed to understand the spatially resolved star formation histories (SFH) of galaxies (Cid Fernandes et al. 2013, 2014; López Fernández et al. 2016). Clear evidence that mass-assembly in typical galaxies progresses inside-out (Pérez et al. 2013). The SFH and chemical enrichment of bulges and early-type galaxies are fundamentally related to their total stellar mass, while for disk galaxies they are more closely related to the local stellar mass density (González Delgado et al. 2014b,a, 2015). Negative age gradients indicate that quenching is progressing outwards in massive galaxies (González Delgado et al. 2015),

and age and metallicity gradients suggest that galaxy bars have not significantly altered the SFHs of spirals (Sánchez-Blázquez et al. 2014). Finally, we explored spatially resolved stellar populations and star formation across the Hubble sequence (González Delgado et al. 2015, 2016), and how mergers influence the assembly of blue ellipticals (Haines et al. 2015). ii) We studied the origin of the low intensity, LINER-like, ionized gas in galaxies. These regions are clearly not related to recent star-formation activity, or to AGN activity (Singh et al. 2013). They are most probably related to post-AGB ionization in many cases (Kehrig et al. 2012; Papaderos et al. 2013; Gomes et al. 2016). iii) We explored aperture and resolution effects affecting larger single-fiber (like SDSS) and IFS surveys (like MaNGA and SAMI Bundy et al. 2015; Croom et al. 2012). We explored the effects of signal dilution in IFS data obtained for higher redshift galaxies in different gas and stellar population properties (Mast et al. 2014), and proposed a new empirical aperture correction for SDSS data (Iglesias-Páramo et al. 2013, 2016). We also compared average stellar and ionized gas properties with spatially resolved ones (e.g. González Delgado et al. 2014b, 2015); iv) we studied the kinematics of the ionized gas (García-Lorenzo et al. 2015), the effects of bars on the kinematics of galaxies (Barrera-Ballesteros et al. 2014; Holmes et al. 2015), the effects of the interaction stage on the kinematic signatures (Barrera-Ballesteros et al. 2015a), and measured the bar pattern speeds in late-type galaxies (Aguerri et al. 2015). v) We extended measurements of the angular momentum of galaxies to previously unexplored ranges of morphology and ellipticity (e.g., Falcón-Barroso et al. 2015) and proposed a new dynamical classification scheme for galaxies Kalinova et al. (2015). The stellar dynamics together with detail analysis of the stellar populations revealed a tight relation between the initial mass function (IMF) and the local metallcity (Martín-Navarro et al. 2015) and allowed us to dynamically constrain the shape of the IMF in early-type galaxies (Lyubenova et al. 2016). vi) We explored in detail the impact of galaxy interactions on the enhancement of star-formation rates (SFR) and the ignition of galactic outflows (Wild et al. 2014; Barrera-Ballesteros et al. 2015b). vii) We studied the nature of the progenitors of SNe (Galbany et al. 2014); viii) we explored star formation indicators for extended objects and the suitability of Hα as an SFR tracer (Catalán-Torrecilla et al. 2015), as well as the spatially resolved SFR density across the Hubble sequence (González Delgado et al. 2016). ix) We studied oxygen abundance gradients in the gas, developing new calibrators (Marino et al. 2013), finding a characteristic shape (Sánchez et al. 2014; Sánchez-Menguiano et al. 2016), and a weak dependence of the profile truncations on the gradient properties (Marino et al. 2016) and the stellar populations (Ruiz-Lara et al. 2016). x) We explored the mass–metallicity relation for both the stellar populations (González Delgado et al. 2014a) and the gas oxygen abundance (Sánchez et al. 2013). We could not confirm a secondary relation between the SFR and the Metallicity (Sánchez et al. 2015). xi) Finally, we found that many of the global scaling relations such as the star formation main sequence or the mass–metallicity relation are mirrored by local relations that hold on a scale of ~1 kpc (e.g., Sánchez et al. 2013; Cano-Díaz et al. 2016).

CALIFA was designed as a legacy survey, and therefore we have distributed the data in successive data releases (DR) as the number of observed objects has increased and the processing pipeline has improved (DR1 and DR2, Husemann et al. 2013; García-Benito et al. 2015, respectively). These publicly accessible data have already allowed the exploration of several different scientific avenues not addressed by the collaboration (e.g.,

Holwerda & Keel 2013; De Geyter et al. 2014; Martínez-García et al. 2014; Davies et al. 2014; Roche et al. 2015; Ho et al. 2015). In this article we present the third and final data release (DR3) comprising all observations with good quality. We distribute 1576 datacubes corresponding to 667 galaxies, 646 of them observed with the V500 setup, 484 observed with the V1200 setup and 446 combined (COMBO) cubes.

The properties of the galaxies in the DR3 sample are described in Sect. 2. We describe the observing strategy and setup (Sect. 3), processing (Sect. 4), structure (Sect. 5), and data (Sect. 6), which comprise essential information for any scientific analysis of the distributed CALIFA data. Several interfaces to access the CALIFA DR3 data are explained in Sect. 7.

2. The CALIFA DR3 sample

There are two fundamentally different samples of galaxies in the CALIFA DR3: (1) Galaxies that were targeted because they were part of the CALIFA mother sample that is fully described and characterized in Walcher et al. (2014). This sample is called the CALIFA Main Sample. (2) The CALIFA Extension Sample, which is a heterogeneous set of galaxies observed for various reasons as part of different ancillary science projects within the CALIFA collaboration. The DR3 release is the combination of the Main Sample and the Extension Sample.

2.1. Main sample

The Main Sample contains all galaxies for which cubes are released in the CALIFA DR3 and that have been drawn from the CALIFA mother sample.

2.1.1. Mother sample – a recap

The CALIFA mother sample consists of 937 galaxies drawn from SDSS DR7. In earlier papers Walcher et al. (in particular 2014) we quoted the number 939, because we included the galaxies NGC 5947 and NGC 4676B. However, these galaxies did not formally satisfy the selection criteria of the mother sample but were added by hand. We therefore now shifted them to the Extension Sample, where they have a natural place.

The main criteria for the target selection of the mother sample are fully described in Walcher et al. (2014). Briefly for completeness, they are:

– angular isophotal diameter $45'' < \mathrm{iso}A_r < 79.2''$;
– redshift range $0.005 < z < 0.03$;
– Galactic latitude $|b| > 20°$;
– flux limit petroMag$_r < 20$;
– declination $\delta > 7°$.

The lower redshift limit was imposed so that the mother sample would not be dominated by dwarf galaxies. CALIFA thus has a natural lower completeness limit in mass. The upper redshift limit was imposed to keep relevant spectral features observable with a fixed instrumental setup. This limits the total volume probed by the CALIFA sample to roughly 10^6 Mpc^3. Because massive galaxies are very rare, this volume effectively sets the upper mass boundary of the CALIFA sample (and not the diameter selection). The 95% completeness limits of the mother sample are studied in detail in Walcher et al. (2014) and are as follows: $-19 > M_r > -23.1$ in luminosity and $10^{9.7}$ and $10^{11.4}$ $M_\odot$ in stellar mass (with a Chabrier IMF, Chabrier 2003).

In Walcher et al. (2014) we showed that the mother sample has well understood properties. In particular, the diameter selection can be translated into V_{max} values according to the formalism of Schmidt (1968). This allows us to construct the luminosity function from the mother sample and to show that it agrees with the standard literature determination of the luminosity function within the limits imposed by the sample size. Indeed, while the selection effects are understood and can be corrected within our completeness limits, the finite sample size of CALIFA still implies that some galaxy classes have less representatives within the sample. Specifically for the CALIFA Main Sample, the statistics are best for galaxies with stellar masses around $10^{10.8}$ $M_\odot$.

2.1.2. Definition of the main sample

Galaxies were selected for observation from the mother sample randomly, i.e., based only on visibility. We can therefore assume that the Main Sample is a random subset of the mother sample. Below we will proceed to verify this assumption. We base our verification on the same galaxy physical properties studied in Walcher et al. (2014). For DR3 we have re-compiled the catalogues of physical properties for two reasons: (1) we introduced a few bug fixes in column names or with single numbers in the catalogues. (2) We computed new properties based on SDSS Petrosian magnitudes to allow for comparison with the Extension Sample. All tabulated properties are available for all galaxies of the mother sample, i.e., by definition for all main sample galaxies in the release.

The Main Sample as used below contains all galaxies with either a V500 and/or a V1200 cube released in this data release and no quality control flags that mark them as unusable (see Sect. 6.4). The number of galaxies in the main sample is 542.

2.2. Extension sample

The extension sample consists of an inhomogeneous collection of galaxies observed in the CALIFA setup, but not following the same sample selection criteria of the mother sample. This means in particular that V_{max} values cannot be computed for the extension sample. On the other hand, extension sample galaxies have mostly been selected to cover galaxies that are intrinsically rare and thus not found in the CALIFA Main Sample. They thus provide useful benchmarks for such rare galaxies.

The CALIFA setup is used in the observations of the extension sample galaxies, i.e., the same gratings, grating angles, exposure times and observing strategy. However, many extension programs did not select galaxies from the SDSS DR7 imaging survey. This imaging is needed to ensure good photometric calibration (Sect. 4.1). Thus, for all extension programs, the additional selection criteria of being in the SDSS footprint and of fulfilling the quality control (QC) requirements (Sect. 6) are imposed.

2.2.1. Dwarf galaxies

The extension program on dwarf galaxies is led by García-Benito. The galaxies in this program have CALIFA IDs between 1000 and 1999. The project aims to observe a statistically meaningful sample of dwarf galaxies in the local Universe ($9 < D < 40$ Mpc). The sample was selected to be a magnitude-limited sample of local field galaxies observed with SDSS and

covering a similar observed magnitude range as the CALIFA main sample.

The following selection criteria were used: i) the size of the galaxy (optical diameters) fill the PPak FoV, i.e., $29.7'' < \text{iso}A_r < 79.2''$; ii) the ratio of the minor to major axis $\text{iso}B_r/\text{iso}A_r > 0.6$, so that the galaxies are found to be almost face on; iii) $M_r > -18$ iv) $z > 0.002$.

The input sample contained a total of 82 objects of which 34 were observed and included in the CALIFA DR3.

2.2.2. Pairs and interacting galaxies

The extension program on pairs and interacting galaxies is led by Barrera-Ballesteros. The galaxies in this program have CALIFA IDs between 2000 and 2999. The project aims to complete the IFU data for those pairs where only one companion galaxy was included in the CALIFA mother sample. The sample was selected to include companions of a CALIFA main sample galaxy with: i) a projected distance of 160 kpc; ii) a systemic velocity difference of less than 300 km s^{-1}; ii) an r-band magnitude difference of less than 2 mag. For details of the CALIFA pair selection see Barrera-Ballesteros et al. (2015b).

This sample also includes the second galaxy of the "mice" (NGC 4676B) as ID number 2999. This galaxy was observed in the time allocated to the main survey since it seemed worthwhile to cover the full "mice" merger. These data have been published in (Wild et al. 2014).

In total there are 29 galaxies from this program in the CALIFA DR3.

2.2.3. Low- and high-mass early-type galaxies

The extension program on early-type galaxies (ETGs) is led by van de Ven, Lyubenova & Meidt. The galaxies in this program have IDs between 3000 and 3999. This extension contains are three subprograms with the following scientific aims: a) studying the dark matter content of low-mass ETGs; b) constraining the IMF in high-mass ETGs; and c) testing fading scenarios for low-mass early-type spirals.

The selection criteria for the low-mass ETGs were: a) $9.4 < \log(M*/M_\odot) < 10.4$; b) $35'' < \text{iso}A_r < 79.2''$; c) declination $\delta > 7°$ and $75° < \text{RA} < 300°$; and d) concentration $r_{90}/r_{50} > 2.8$; visual inspection to remove non-ETGs. The selection criteria for the high-mass ETGs were: a) $\log(M*/M_\odot) > 11.4$; b) $35'' < \text{iso}A_r < 79.2''$; c) declination $\delta > 7°$ and $75° < \text{Right Ascension RA} < 300°$; d) concentration $r_{90}/r_{50} > 2.8$; and e) visual inspection to remove non-ETGs. The selection criteria for low-mass early-type spirals were: a) $9.0 < \log(M*/M_\odot) < 10.0$; b) $30'' < \text{iso}A_r < 80''$; c) declination $\delta > 7°$; d) inclination = $\text{acos}(1-\text{iso}B_r/\text{iso}A_r) < 80°$; e) morphological types S0, Sa and Sb; and f) preference to those with literature HI observations.

For all three subsamples the number of available galaxies was then reduced further by visibility at the scheduled time of observation. There are 36 galaxies from this program in the CALIFA DR3.

2.2.4. Pilot studies

Those galaxies with IDs in the range 4000–4999 were extracted from CALIFA pilot studies and are fully described in Mármol-Queraltó et al. (2011). Most of the pilot study galaxies were observed with either the V300 or the V600 gratings and can therefore not be included in this homogeneous data release. The pilot

studies targeted spiral galaxies with low inclinations to study the properties of the HII regions, as described in Sánchez et al. (2012b).

Note that the galaxy with ID number 4034, NGC 5947, is a galaxy from the pilot study sample that was observed as part of the main sample as described in Walcher et al. (2014). There are 3 galaxies from this program in the CALIFA DR3, including NGC 5947. Those are only ones included in the Pilot Sample that were observed with the final CALIFA configuration and are part of the SDSS imaging survey (a pre-requisite for being distributed in this data release). All the three fulfill the quality control criteria.

2.2.5. Supernova environments

The extension program on core collapse supernova (CCSN) environments is led by Galbany. The galaxies in this program have IDs between 5000 and 5999. The project aims to get imaging spectroscopy for low-mass galaxies that hosted Type Ib, Ic and II supernovae with available light curves. This sample increases the completeness of the SN host galaxy sample from the CALIFA Survey presented in Galbany et al. (2014) and Galbany et al. (2016), which has a deficit of CCSNe in low-mass ($\lesssim 10^{10}\ M_\odot$) galaxies.

Objects were selected from the Asiago SN catalog[1] (Barbon et al. 1999) following these criteria: a) SN projected galactocentric distance lower than 40 arcsec, in order to cover the local SN environment; b) systemic velocity of the galaxy lower than 9000 km s^{-1} ($\sim z < 0.03$); c) log D_{25} (decimal logarithm of the apparent 25 mag/arcmin^2 isophotal diameter) lower than 1.12, which corresponds to galactic radius lower than 40 arcsec; d) declination $\delta > 0°$; and e) SN light curve publicly or privately available.

The input sample contains a total of 49 objects of which 14 were observed and included in the CALIFA DR3.

2.2.6. Compact early-type galaxies

The extension program on compact early-type galaxies is led by Yıldırım and van den Bosch and includes galaxies with CALIFA IDs between 9000 and 9999. The scientific aim is the characterization of extremely compact host galaxies of supermassive black holes. Galaxies were selected from the HETMGS (*Hobby-Eberly* Telescope Massive Galaxy Survey, van den Bosch et al. 2015) to have: i) large black hole spheres of influence; ii) 2MASS half-light radii smaller than 2 kpc; iii) very high central density as measured by the velocity dispersion over central resolution element ($\sigma/1''^2$). Scientific results and further descriptions of the sample can be found in Yıldırım et al. (2015, 2016). In those papers, the data are deeper than the standard CALIFA depth, as the exposure times are four times longer. For the sake of uniformity of the DR3, we limit ourselves to the standard CALIFA depth, i.e., exposure time. Observations are taken with the V500 low-resolution setup only.

Only 7 of the 17 galaxies are included in this data release as the remainder lack SDSS imaging needed for the CALIFA pipeline.

2.2.7. Other extension programs

There are two galaxies in DR3 from extension programs that yielded only one released cube, and it is therefore not useful to
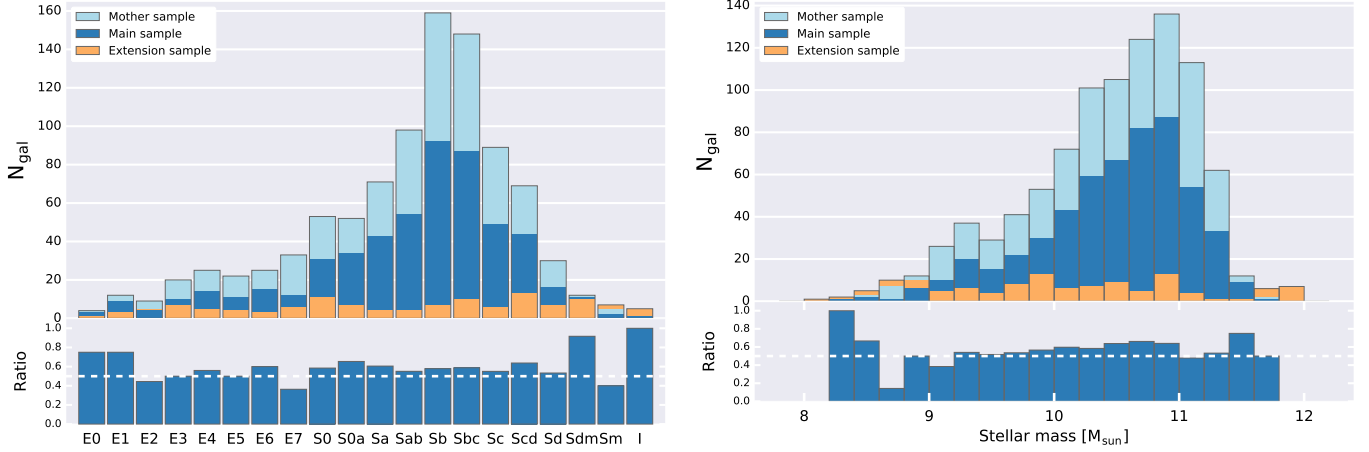
---

[1] http://graspa.oapd.inaf.it/asnc.html

Fig. 1. *Left panel*: histograms of visual morphological classification in the DR3 samples. *Right panel*: stellar mass histogram. The lower portion of each panel shows the ratio between the main sample and the mother sample.
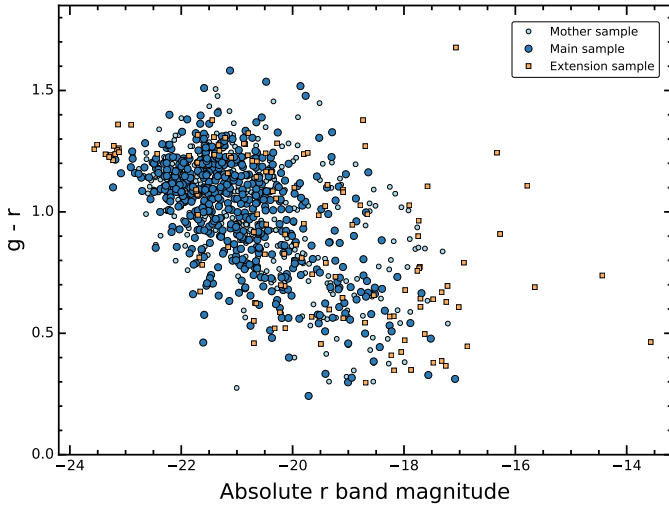

Fig. 2. Distribution of DR3 galaxies in the color magnitude diagram.

describe these programs in detail. The galaxy with CALIFA ID number 7001 is CGCG263-044, classified as Sb in NED, is relatively edge-on and classified as a Type 2 AGN. The galaxy with CALIFA ID number 8000, NGC 426, is a massive galaxy, classified as a cD.

2.3. Properties of the released galaxies

The physical properties each galaxy in each sample, including its name, CALIFA ID, coordinates, redshift, photometry, morphology, and stellar mass are available from the DR3 web page.

As clearly seen in Fig. 1, the morphological and stellar mass distributions of the main sample are consistent with those of the mother sample. While larger differences are seen at low stellar masses, this follows from the low number of galaxies overall in this mass range. This test therefore implies that the selection of main sample galaxies from the mother sample using target visibility preserves the mother sample statistics.

Figure 2 shows the distribution of galaxies in the color-magnitude diagram. Again, the good coverage of the color-magnitude diagram found for the mother sample is retained for the main sample. The Extension Sample *by design* covers those

regions that were not included in the mother sample, i.e., the bright end of the red sequence and dwarf galaxies.

In Walcher et al. (2014) we reported on the average spatial coverage of the mother sample galaxies by the IFU as a fraction of the Petrosian half light radius (SDSS pipeline quantity PetroR50) r_{50} as computed from the growth curve photometry. About 97% of all galaxies are covered out to at least $2 \times r_{50}$. This statement holds for the main sample as well. Because growth curve photometry is not available for the Extension Sample, we refer here to the SDSS Petrosian half light radius, which we will denote as r_e^p. The average spatial coverage in terms of r_{50} is 4.2 for the main sample and 7.9 for the Extension Sample, with the broader coverage of the Extension Sample being driven by the inclusion of dwarf galaxies therein. All Extension Sample galaxies are covered out to the SDSS isophotal major axis, as is the case for the main sample.

Figure 3 shows the distribution of galaxies from the main sample and Extension Sample in the redshift-magnitude and redshift-size diagrams. Clearly, galaxies slightly larger than the CALIFA size limit are so rare that they are under-represented within the CALIFA volume *independently of their size*. Finding them requires an extension to higher redshift. Galaxies smaller than the CALIFA size limit are abundant in the local Universe. These dwarf galaxies were not included in the mother sample *by design* to avoid swamping the main sample with them. The dwarf galaxies in the Extension Sample somewhat helps to circumvent this self-imposed limitation. Still, a dedicated dwarf imaging spectroscopy survey of similar size to CALIFA is missing in the literature.

2.4. Luminosity functions of the main sample

In Walcher et al. (2014) we established that the luminosity function of the CALIFA mother sample compares well with the reference SDSS sample of Blanton et al. (2005). We now investigate whether the same statement can be made for the main sample. For all technical details on how the luminosity functions are obtained and for the derivation of the CALIFA mother sample completeness limit at $M_r \approx -19$ we refer the reader to Walcher et al. (2014).

The only difference in the derivation of the luminosity function for the main sample is that the available volume has been made smaller by a random subselection from the mother sample. To correct for this, one needs to multiply the V_{max} values of
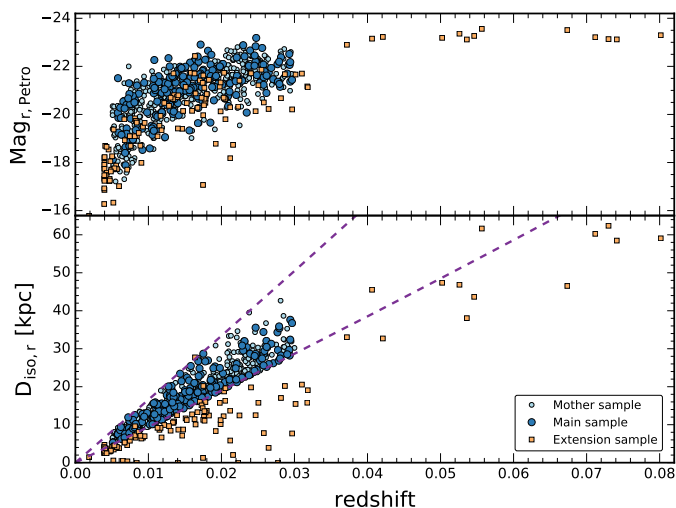
Fig. 3. Distribution of DR3 galaxies in the redshift-magnitude (*upper panel*) and redshift-size (*lower panel*) diagrams.
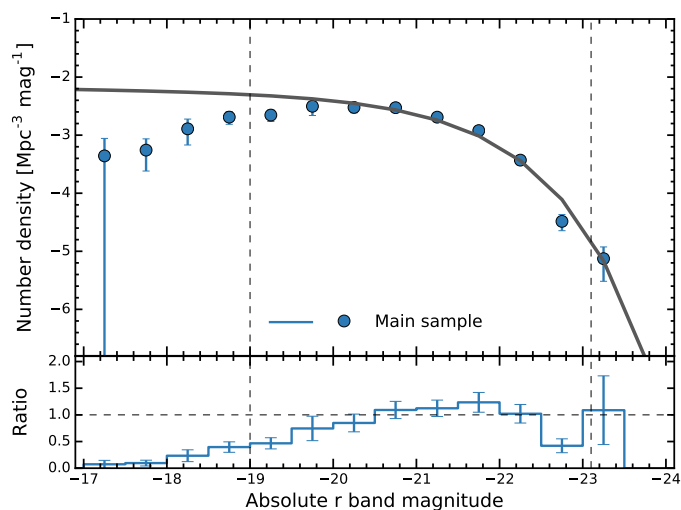

Fig. 4. *Top panel*: *r*-band luminosity functions for the SDSS reference sample from Blanton et al. (2005; solid line) and the DR3 main sample. Error bars represent Poissonian uncertainties. *Bottom panel*: ratio between the main sample and SDSS.

the main sample galaxies with a ratio of the number of galaxies in the sample in use (e.g., 542 in the case of the full main sample) divided by the number of galaxies in the mother sample (937). The precondition for this simple procedure is that the sub-sample in use can be considered a random subset of the mother sample. We compared the mass and morphology distributions of the main sample and the mother sample using a χ^2 test and found that the probability that they were drawn from the same distributions are 98% and 97%, respectively. Thus we conclude that the main sample is a random subselection from the mother sample.

Figure 4 shows the *r*-band luminosity function of the DR3 main sample compared to the Schechter function derived in Blanton et al. (2005). Within the statistical uncertainties, the DR3 main sample reproduces the standard luminosity function. There are two points at the limits of our completeness range (at −19.25 and −22.75 in absolute magnitude) that seem to deviate more than the 1σ range of their errorbars. It is not possible to formally decide whether this indicates a (small) issue with our

completeness or whether this is just as expected from statistics (~30% of points should lie outside the 1σ errorbar). In any case, a formal χ^2 test indicates a probability of 99.9% that the two functions are identical. We thus conclude from this section that the main sample is representative of the galaxy population within the same limits indicated in Walcher et al. (2014). This is an important result that allows the use of CALIFA data to construct galaxy distribution functions in all scientifically useful parameters. One should keep in mind, however, that not all mass ranges are equally well sampled statistically.

3. Observing strategy and setup overview

The observing strategy and setup of the CALIFA survey were described in detail in Sánchez et al. (2012a) and have not changed during the survey's six year duration. For the sake of completeness, we provide here a very brief summary.

All galaxies were observed using PMAS (Roth et al. 2005) in the PPak configuration (Verheijen et al. 2004; Kelz et al. 2006). The PPak science bundle was created to cover a wide area on sky following the requirements of the Disk Mass Survey (Bershady et al. 2010), and is now a common-user instrument. The PPak Integral Field Unit (IFU) has a Field of View (FoV) of $74'' \times 64''$ and it contains a total of 382 fibers, distributed in three different groups. 331 "science" fibers are arranged in a hexagonal grid, with each fiber projecting to $2''.7$ in diameter on the sky. The fiber-to-fiber distance is $3''.2$, which yields a total filling factor of ~60%. An additional set of 36 fibers located in a ring with radius $72''$ measure the surrounding sky background. Finally, 15 fibers are connected to the calibration unit.

The goal of CALIFA was to observe every sample galaxy using two different overlapping setups. The red low-resolution setup (V500; $R \sim 850$) covers the wavelength range 3745–7500 Å. The spectra on the CCD are affected by internal vignetting within the spectrograph, giving an unvignetted range of 4240–7140 Å. The blue mid-resolution setup (V1200; $R \sim 1650$) covers the range 3400–4840 Å, with an unvignetted range of 3650–4620 Å. The resolutions quoted are those at the overlapping wavelength range ($\lambda \sim 4500$ Å). However, since observing in the V1200-setup was more time consuming and required more restrictive weather conditions, not all galaxies were finally observed in both setups. For those that were observed in both setups, the quality control rejected a larger fraction.

A three pointing dithering scheme was used for each object in order to reach a filling factor of 100% across the entire FoV of the science fibers. The dither comprises the following pattern of offsets: (0, 0), (−5.22, −4.53), and (−5.22, 4.53), in arcsec with respect to the nominal position of the galaxy. This pattern comprises a jump of two inter-fiber distances instead of one to avoid sampling the same area on sky with the same fiber. We thus minimize the effects of low transmission fibers in the final dataset.

The exposure times per pointing were fixed, and have been selected to match the signal-to-noise (S/N) requirements of Sánchez et al. (2012a). We carried out V1200 observations during dark nights with an exposure time of 1800 s per pointing (split into 2 or 3 individual exposures). We obtained V500 observations during gray nights with 900 s per pointing.

For the observations of the main sample, target galaxies were randomly selected from the mother sample. The strategy for observing extension sample galaxies was more varied, and depended on the extension program. Altogether, 685 galaxies were observed during the last 6 yr, making use of 237 clear equivalent nights distributed between the 6th of June 2010 and the 16th of

April 2016. The number 237 is obtained from 176 totally clear nights, plus observations distributed in partially clear nights or among other service programs. Data cubes for 667 of these are in DR3, following strict quality control procedures.

In the following section, we describe the improvements to the CALIFA data reduction pipeline used to produce the DR3 data.

4. Data processing and error propagation

4.1. Overview of the reduction scheme

The CALIFA data reduction was performed by a semi-automatic pipeline that follows the procedures for the reduction of fiber-fed IFS data described in Sánchez (2006). The CALIFA data reduction pipeline was first (until V1.2) developed in `Perl` and using R3D[2]. It was then rewritten using a `Python`-based core in the Py3D package (V1.3c and V1.5 Husemann et al. 2013; García-Benito et al. 2015). The current pipeline version, V2.2, has now fully replaced the original scheme and uses `Python` for the full process.

The reduction process comprised the following steps: i) the four different FITS files created by the amplifiers of the detector were re-arranged into a single frame, which is then bias subtracted. Cosmic rays were removed and masked according to Husemann et al. (2012); ii) relative offsets in the tracing due to flexure were estimated with respect to the continuum and arc-lamp calibration frames and the wavelength solution was applied to each individual science frame; iii) the stray-light map was reconstructed using the gaps between the fiber traces[3] and subtracted from the calibration and science exposures; iv) an optimal extraction algorithm (Horne 1986) was used to extract the spectra based on measurements of the positions and widths derived from the continuum lamp. The optimal extraction relies on a good characterization of the shape of the spectra along the cross-dispersion axis. In theory it is required to make a measurement considering both the Gaussian core and the Lorentzian wings. However, in practical terms the adopted procedure to subtract the stray-light removes most of the Lorentzian wings, and therefore a pure Gaussian function is a good representation of the shape of the spectra; v) the extracted flux for each pixel in the dispersion direction was stored in a row-stacked-spectrum (RSS) file; vi) the spectra were resampled to a linear grid in wavelength using the wavelength solution and resolution obtained from the HeHgCd calibration lamp exposure taking for each pointing, taking into account possible flexure offsets in the dispersion axis within each pointing; vii) in the same step, the spectral resolutions were homogenized to a common value along the dispersion axis using an adaptive Gaussian convolution kernel.

The Poisson shot noise, the read-out noise, and bad pixel masks were propagated in the reduction process. For the wavelength solution, errors were analytically propagated during the Gaussian convolution and a Monte Carlo approach was used to estimate the noise vector after the spline resampling of the spectra. Fiber-to-fiber transmission throughput was corrected using an RSS master fiberflat created from sky exposures taken during twilight on all survey observing nights.

Flux calibration was performed using the procedure described in García-Benito et al. (2015). In essence we performed a

dedicated calibration program, re-observing two dozen CALIFA ETGs chosen as secondary calibrators and a set of the standard stars with the PMAS Lens-Array (LArr; Husemann et al., in prep.). This IFU covers a continuous $16'' \times 16''$ FoV which produces highly accurate spectrophotometric spectra. Comparing the photometry of the calibrated LArr data with aperture-matched SDSS photometry in the *g* and *r*-bands, the absolute spectrophotometric accuracy of our standard galaxies is <0.03 mag.

During the last 4 years of the survey (2012–2015) we were observing the ETG calibration galaxies regularly, and updating the master sensitivity curve of the instrument/setup created as described in García-Benito et al. (2015). We adopted that sensitivity curve to perform the spectrophotometric calibration for DR3. For each particular pointing the flux calibration was performed by correcting for the atmospheric extinction using the mean observatory curve presented by Sánchez et al. (2007), and using the extinction (A_V) provided by the Calar Alto Vistual EXtinction monitor (CAVEX) measured at the moment of the observations. When the CAVEX was not operating (~15% of the time) we adopted the average extinction at the observatory ($A_V \sim 0.15$ mag). Most of the remaining systematic effects in the spectrophometric uncertainty for CALIFA are driven by the uncertainties in the wavelength-dependent atmospheric extinction at the time of each observation, that is not properly monitored at the observatory.

The science spectra corresponding to the three dithered exposures were combined into a single frame of 993 spectra, following the registration procedure described in García-Benito et al. (2015). In summary, we computed the flux corresponding to the 331 apertures of the fibers for each pointing from sky-subtracted SDSS DR7 images in the bands covering the wavelength of our observation. The apertures were shifted in right ascension and declination over a search box around the nominal coordinates of the pointing and the best registration was found on the basis of a χ^2 comparison between the SDSS aperture-matched fluxes and those derived from the RSS spectra themselves. This provided us with accurate astrometry for each pointing (with a typical error of ~0.2''), and a flux recalibration pointing by pointing. This recalibration anchors the absolute CALIFA spectrophotometry to that of the SDSS DR7.

After the Galactic extinction correction (Schlegel et al. 1998; Cardelli et al. 1989), the RSS was ready for the spatial rearranging of the fibers and creation of the datacube. We used a flux-conserving inverse-distance weighting scheme to reconstruct a spatial image with a sampling of 1'' using the same parameters as described in García-Benito et al. (2015). This scheme is now adopted by other IFU surveys such as MaNGA (Bundy et al. 2015), as described by Law et al. (in prep.). First, we reconstructed the datacube and estimated the differential atmospheric refraction (DAR) offset. In a second step, we reconstructed the cube again but shifting the position of the fiber at each wavelength against the regular grid according to the DAR offset measured in the first reconstruction. This two-stage iteration avoids one resampling step, which is important for accurate error propagation.

4.2. Improvements to the CALIFA data reduction scheme

The main improvements to the pipeline when going from V1.5 (DR2) to V2.2 (DR3) are: i) a new version of the high-level scripting code that handles the night-by-night reduction; ii) an improved version of the COMBO datacubes, i.e., the cubes created by combining the datasets from the V500 and V1200 setups

---

[2] http://www.astroscu.unam.mx/~sfsanchez/r3d/
[3] See Kelz et al. (2006) for a description of the spatial arrangement of the fibers on the pseudo-slit and CCD.

(already used in different science studies, e.g. González Delgado et al. 2015, 2016); iii) fully automatic verification of the registration and astrometry process; iv) a second-order correction of the datacube reconstruction based on a comparison with the SDSS images.

As indicated before, the new high-level routines that handle the reduction are now written in Python 2.7. Like in the previous version the low-level routines of the reduction are based on the Py3D package, and therefore the reduction sequence and detailed routines have not changed since V1.5 (García-Benito et al. 2015). The use of Python for the high-level routines provides three basic improvements: i) portability, i.e., the pipeline can be easily installed on any workstation, which is more user friendly; ii) maintenance, i.e., future updates to the pipeline will be easier; and iii) speed, thanks to the multi-processing module. Basically all objects of the same type (science objects, calibration stars, etc.) observed during a night can be processed in parallel.

The pipeline creates a new version of the COMBO cubes by taking into account the data from both the V500 and V1200 setups in the overlapping areas of the spectrum. These COMBO cubes are created to solve the problem of vignetting affecting both setups at the edge of their spectral wavelength ranges (Sect. 4.2 of García-Benito et al. 2015). The COMBO cubes span an unvignetted wavelength range of 3700–7140 Å.

In the previous version (not distributed in DR2 and DR3), the COMBO cubes were created by glueing the data from both datasets together at a cut-off wavelength. Specifically, the resolution of the V1200 cube was degraded to that of the V500 cube and the cubes were recentered. Then, the resolution-matched V1200 cube was used below a cut-off wavelength of 4500 Å. Above that wavelength the V500 cube was used. In order to avoid low-level spectrophotometric mismatches the V1200 spectra were re-scaled to the V500 ones by the average of the ratio between both datasets in the overlapping wavelength range.

The COMBO cubes in DR3 were created by using the spectra from both setups in the overlapping region simultaneously. Like in the previous case, the V1200 data were spatially recentered, flux rescaled and degraded in resolution to match the V500 data. Then the COMBO cube was created by averaging the spectra corresponding to each dataset in the overlap region, weighted by the inverse of the cube error. For the remaining wavelength range the COMBO cube consists of only the V1200 or the V500 spectra. This new procedure improves the S/N in the overlap region of the COMBO cubes.

The current spatial registration scheme is the same as the one described in García-Benito et al. (2015). It is known that this registration process fails in some cases, particularly in low surface brightness and/or edge-on galaxies or in the presence of bright foreground field stars. These failures happened more frequently in the V1200 setup, given its lower S/N on average compared to that of the V500 setup. The current V2.2 pipeline automatically discards the registration procedure when the minimum χ^2 is higher than a given threshold. Then it only applies a global flux re-scaling as described in Husemann et al. (2013), relying on the nominal offsets provided by the telescope for the World Coordinate System (WCS Greisen & Calabretta 2002). A boolean header keyword (REGISTER) is added to the datacube to indicate whether the cube has been fully registered or not. In García-Benito et al. (2015) we found that the astrometric solution has an accuracy better than 3″ for ~93% of the targets. We repeated the analysis for the new dataset and we find that there is a better precision in our astrometry, with a standard deviation in the offset with respect to the SDSS one of ~0.6″ in both RA and Dec. However, we have a systematic offset of −0.6″ in both

directions (e.g., RA$_{CALIFA}$ − RA$_{SDSS}$), whose source is still unclear.

Finally, a second-order correction was applied to the CALIFA datacubes to match their spectrophotometry as much as possible to that of the SDSS images. This procedure followed a two-step process. First, a second-order correction to the WCS astrometry of the cubes was obtained. Sky-subtracted SDSS DR7 g- (for the V1200) and r- (for the V500) band images were downsampled to 1″/pixel. The corresponding images using the proper filter response curve were created from the CALIFA datacubes. The synthetic CALIFA image and SDSS image were registered using a Discrete Fourier Transform and the offsets are updated in the CALIFA image and cube headers. We then convolved the SDSS image with a sequence of circular Moffat kernels,

$$I(r) = I_0 \left[1 + \left(\frac{r}{\alpha} \right)^2 \right]^{-\beta},$$
(1)

varying α and β, i.e., effectively varying the Full Width Half Maximum (FWHM), which depends on both parameters,

$$FWHM = 2\alpha \sqrt{2^{\frac{1}{\beta}} - 1}.$$
(2)

Each convolved SDSS image was then compared to the corresponding reconstructed CALIFA images and the best parameters are selected by χ^2 minimization. This procedure provides the differential spatial resolution between the SDSS images and the CALIFA cubes. Taking into account the FWHM of the Point Spread Function (PSF) for the SDSS images (that on average is ~1.5″) we obtained a first order estimate of the FWHM of the CALIFA PSF for each cube. This is stored in the header keyword FWHM in units of arcsec.

Once the convolved SDSS image that best reproduces the one reconstructed from CALIFA was obtained, we computed their ratio. This ratio, called *SDSSflat*, is a 2D map with a mean value of one and a scatter of a few percent across the FoV. The final correction was applied by multiplying the fluxes and variances of the data with this 2D map, changing the photometric absolute scale in each spaxel, without affecting the shape of the spectra. The flux level of the integrated spectrum for each datacube changed by less than a few percent both in absolute and relative terms (from blue to red), due to the different relative contribution of each individual spaxel to the sum.

The *SDSSflat* is stored in an additional extension in the FITS files named FLAT. In some cases, in particular when there are registration issues and/or very bright field-stars, the procedure fails. This was easily identified during the QC process since the distribution of values within SDSSflat was not symmetric, was not centered on ~1, and its application to the cube modified the shape of the integrated spectrum by more than the expected spectrophotometric accuracy (~3%). In those cases we have preferred not to apply the correction. Whether this correction is applied or not is indicated by a header keyword (FLAT_SDSS), that is set to true or false.

Figure 5 illustrates the improvements and similarities between V2.2 (DR3) and V1.5 (DR2) of the data reduction by comparing i) the g-band images extracted from both datacubes of the galaxy NGC 5406 (ID=648) with the corresponding resolution-matched g-band SDSS image, and ii) the Hα intensity map extracted from both datacubes using the Pipe3D pipeline (Sánchez et al. 2016), together with a narrow-band image centered on the same emission line. This last image was taken with the 4.2 m *William Herschel* Telescope (Roque de los Muchachos Observatory, La Palma, Spain) using the AUXCAM detector
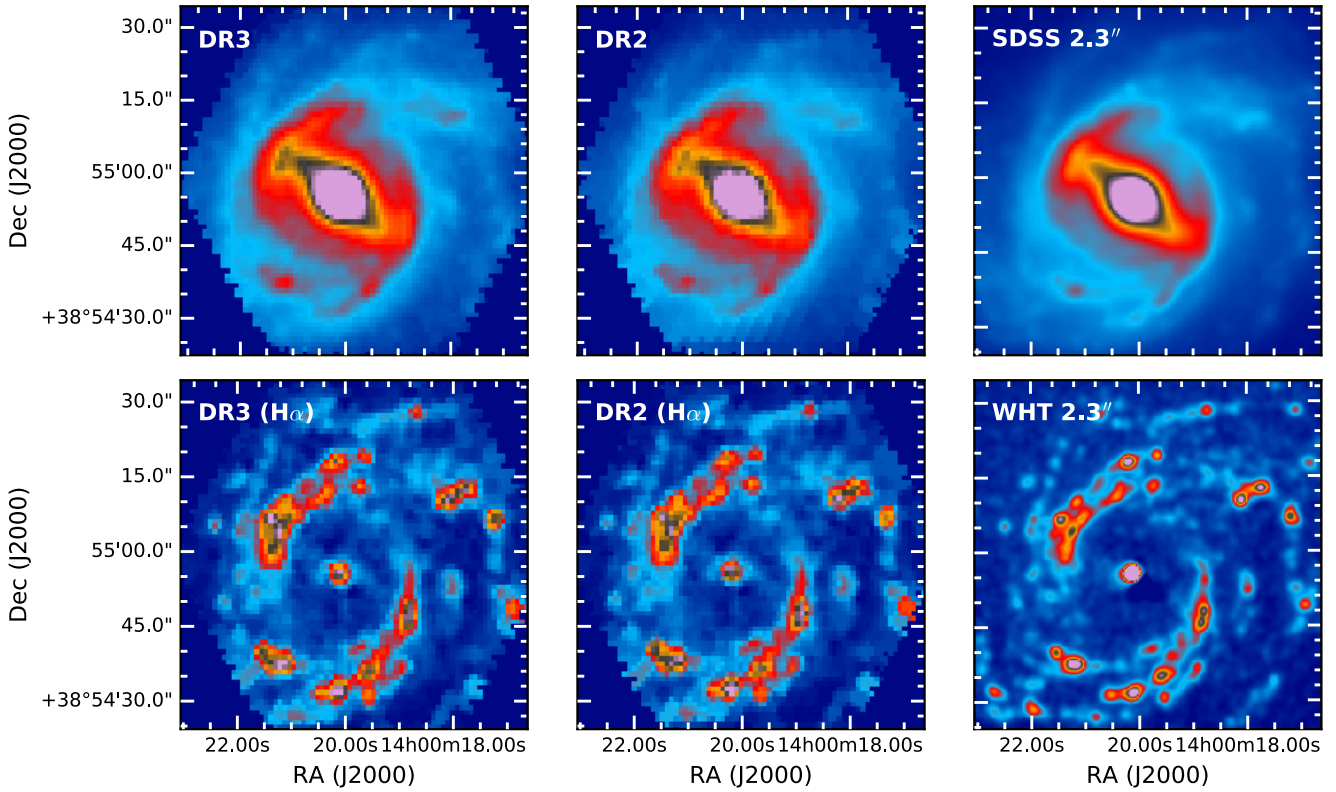
Fig. 5. *Top panel*: comparison between *g*-band images extracted from CALIFA datacubes of the galaxy NGC 5406 (ID=684) created using the V2.2 (DR3) and V1.5 (DR2) pipelines, together with the corresponding SDSS image convolved with a Gaussian function to match the spatial resolution of the CALIFA datacubes. *Bottom panel*: similar comparison between Hα images extracted from the same datacubes using the Pipe3D pipeline, and a resolution-matched Hα image taken with the 4.2 m *William Herschel* Telescope (Roque de los Muchachos Observatory, La Palma, Spain), using the AUXCAM detector (Sánchez-Menguiano et al., in prep.). The FoV has been reduced to match that of CALIFA.

(Sánchez-Menguiano et al., in prep.). The effects of the *SDSSflat* are visible through the absence of patchy structures in the broad-band images from V2.2, evident in the V1.5 image. Finally, the spatial resolution is not affected, as clearly seen in the similarities between the three Hα images.

4.3. Characterization of spatially correlated noise

Like in the case of V1.3c and V1.5 the interpolation procedure used to obtain a regular grid implies that the output pixels in the final datacube are not independent of each other. The Gaussian interpolation method distributes the flux from a given fiber to several pixels, which are combined with neighboring pixels within a certain radius (see Sect. 4 of García-Benito et al. 2015). This causes the noise in the adjacent pixels to be spatially correlated. Recall that even in the case that there is no interpolation of the RSS files, all spectra are correlated at some level due to their projection on the detector. This correlation is stronger in adjacent spectra at the detector level, that are not necessarily adjacent in the focal plane of the telescope (Kelz et al. 2006). This correlation implies that a measurement of the noise in a stacked spectrum of *N* pixels will be underestimated. Characterizing this effect is essential for estimating the statistical errors when spectra in datacubes are coadded.

Following Husemann et al. (2013) and García-Benito et al. (2015) we checked that the error spectra derived from the pipeline for individual spaxels are reliable. Spectral fitting analysis can provide an approximate assessment of the accuracy of the error spectra. In Fig. 6 we update Fig. 9 of
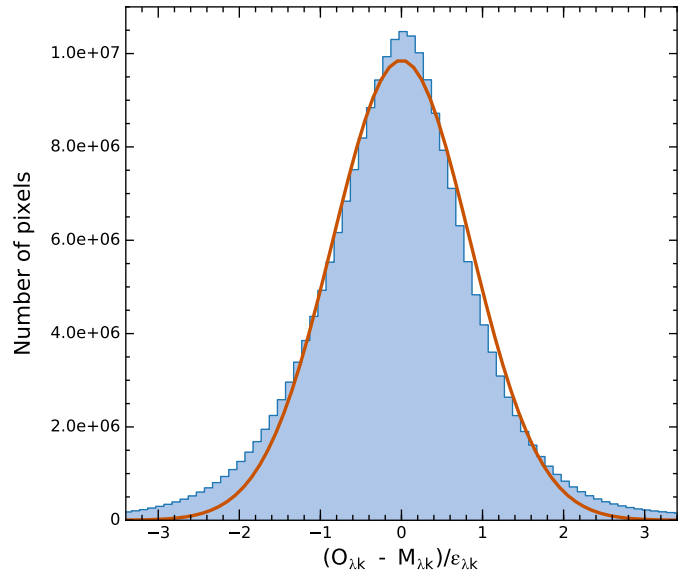

Fig. 6. Histogram of the reduced residuals $(O_{\lambda,k} - M_{\lambda,k})/\epsilon_{\lambda,k}$ for all wavelengths, all bins (*k*) and all galaxies in DR3 (433400381 points in total). The orange line shows the best Gaussian fit to the sample.

Husemann et al. (2013) and Fig. 10 of García-Benito et al. (2015) for DR3 data. The plot shows the histogram of residuals, i.e., the difference between the observed (O_λ) and synthetic (M_λ) spectra obtained with Pipe3D in units of the corresponding error
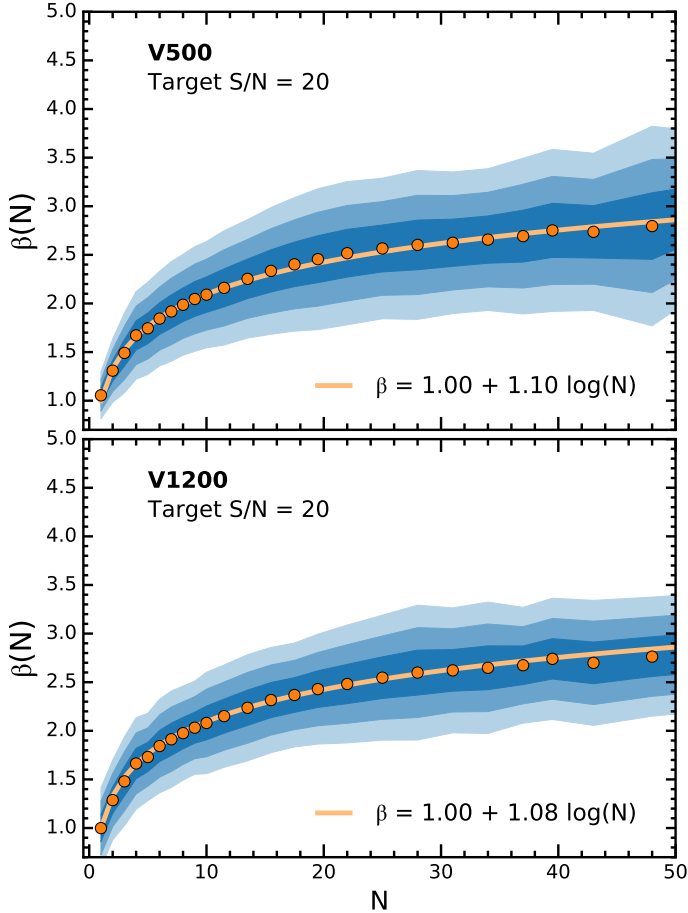
Fig. 7. Noise correlation ratio β (ratio of the real estimated error to the analytically propagated error) as a function of number of spaxels per bin for all the V500 (*top panel*) and V1200 (*bottom panel*) data of DR3 at a target S/N of 20. Shaded areas mark the 1σ, 2σ, and 3σ levels. The orange lines represent the best fitting logarithmic function with a slope $\alpha = 1.10$ and $\alpha = 1.08$, respectively.

ϵ_λ (details of the fitting procedures can be found in Sect. 6.6). The distribution is very well described by a Gaussian centered at 0.01 with $\sigma = 0.83$, only slightly lower than expected if residuals are purely due to uncorrelated noise.

The correlated noise can be taken into account by providing the spatial covariance (Sharp et al. 2015). However, like in DR1 and DR2, a more practical approach consists of using the datacubes to introduce the noise correlation ratio as a function of the number of pixels $\beta(N)$. β is the ratio of the "real" or measured error to the analytically propagated error of the binned spectra as a function of bin size. To calculate β We used the Voronoi adaptive binning method (implemented for optical IFS data by Cappellari & Copin 2003) with a target S/N of 20 to obtain a sample of coadded spaxels covering different numbers of spaxels. We removed individual spaxels with $S/N < 5$ from the analysis, and coadded bins with areas larger than 60 spaxels. The "real" noise was then obtained from the detrended standard deviation in certain defined wavelength windows (see Sect. 6.7). The results obtained for all DR3 datacubes, shown in Fig. 7, can be described well by the following logarithmic function:

$$\beta(N) = 1 + \alpha \log N, \tag{3}$$

where N is the number of spaxels per bin.

The values for the slope α are very similar in both setups, with a value of <1.10 for V500 and 1.08 for V1200, with errors

in the estimation of the slope around 0.01. Both of them agree well with the observed distribution within one sigma. The slope is lower than the DR1 value (mean ~1.4), but very similar to the value reported for DR2. This indicates that the noise in DR3 and DR2 datacubes is less correlated than that in the DR1 datacubes. This is expected since we changed the parameters in the interpolation and the registration procedure from V1.3c to V1.5 and V2.2. Detailed instructions on how to estimate the coadded error spectrum are given in Appendix A of García-Benito et al. (2015).

5. CALIFA data format and characteristics

The CALIFA data are stored and distributed as 3D data cubes in the standard binary FITS format. Each FITS file consists of several Header Data Units (HDUs). These HDUs contain, in order within each FITS file, (1) the measured flux densities, corrected for Galactic extinction as described in Sánchez et al. (2012a), in units of $10^{-16}\,\mathrm{erg\,s^{-1}\,cm^{-2}\,\mathring{A}^{-1}}$ (primary datacube); (2) the associated errors; (3) the error weighting factors; (4) the bad pixel flags; (5) the fiber coverage; and (6) the SDSSflat correction to the interpolation scheme (see also Table 1). This last HDU was absent in DR1 and DR2, as explained in Sect. 4.2. The remaining extensions were explained in detail in Husemann et al. (2013) and García-Benito et al. (2015).

The first two axes of the cubes correspond to the spatial dimension along right ascension and declination with a $1'' \times 1''$ sampling. The third dimension represents the wavelength and is linearly sampled. Table 2 summarizes the dimensions of each datacube (N_α, N_δ, and N_λ), as well as the spectral sampling (d_λ) and resolution (δ_λ).

5.1. Error and weight datacubes

The 1σ uncertainty of each pixel as formally propagated by the pipeline can be found in the first FITS extension. Section 4.3 discusses the accuracy of the uncertainties and their correlation properties. This is important when CALIFA data are spatially binned, and an empirical function is provided to account for the correlation effect. The second FITS extension (ERRWEIGHT) stores the error scaling factor for each pixel in the limiting case that all valid spaxels of the cube would be coadded (see also Appendix of García-Benito et al. 2015). In the case of bad pixels, we assign an error value that is roughly ten orders of magnitude higher than the typical value.

5.2. Bad pixel datacubes

Bad pixel datacubes are stored in the third FITS extension (BADPIX). This information, in combination with the error vector, is essential to properly account for potential problems in each of the pixels. Pixels with flag = 1 report the absence of sufficient information in the raw data due to cosmic rays, bad CCD columns, or the effect of vignetting. They comprise a 4.2% of the total spaxels in the final datacubes. The vignetting effect imprints a characteristic inhomogeneous pattern across the FoV on the bad pixels vector. More details can be found in Fig. 11 of Husemann et al. (2013). These bad pixels have been interpolated over and we strongly suggest not to use them for any science analysis.

Finally, the uncovered corners of the hexagonal PPak FoV are filled with zeros and flagged as bad pixels for consistency.

Table 1. CALIFA FITS file structure.

HDU	Extension name	Format	Content
0	Primary	32-bit float	Flux density in units of $10^{-16}\,\mathrm{erg\,s^{-1}\,cm^{-2}\,\AA^{-1}}$
1	ERROR	32-bit float	1σ error on the flux density
2	ERRWEIGHT	32-bit float	error weighting factor
3	BADPIX	8-bit integer	Bad pixel flags (1 = bad, 0 = good)
4	FIBCOVER	8-bit integer	Number of fibers used to fill each spaxel
5	FLAT	32-bit float	SDSSflat correction to the interpolation

Table 2. Dimension and sampling of CALIFA datacubes.

Setup	$N_\alpha{}^a$	$N_\delta{}^a$	$N_\lambda{}^a$	$\lambda_{\mathrm{start}}{}^b$	$\lambda_{\mathrm{end}}{}^c$	$d_\lambda{}^d$	$\delta_\lambda{}^e$
V500	78	73	1877	3749 Å	7501 Å	2.0 Å	6.0 Å
V1200	78	73	1701	3650 Å	4840 Å	0.7 Å	2.3 Å
COMB	78	73	1901	3701 Å	7501 Å	2.0 Å	6.0 Å

Notes. [a] Number of pixels in each dimension. [b] Wavelength of the first pixel in wavelength direction. [c] Wavelength of the last pixel in wavelength direction. [d] Wavelength sampling per pixel. [e] Homogenized spectral resolution (FWHM) over the entire wavelength range.

The residuals of bright night-sky emission lines are not flagged as bad pixels.

5.3. Fiber coverage datacubes

The inverse-distance weighting that is used to reconstruct the data cubes means that several fibers contribute to each spaxel for most of the spaxels. As explained in García-Benito et al. (2015) we minimized the maximum distance of fibers that can contribute to the flux of a given spaxel to improve spatial resolution. However, the number of contributing fibres for spaxels at the edge of the hexagon defined by the dither pattern is lower than for spaxels inside the hexagon. As a compromise between improved spatial resolution and avoidance of information loss in the outer parts of the hexagon since pipeline V1.5, we also reduced the minimum number of fibers that contribute to each spaxel to one. This extension contains the information on the number of fibers used to compute the flux in each spaxel.

5.4. SDSS flat-fielding image

Pipeline V2.2 has introduced a second-order correction to the interpolation scheme that preserves the spectrophotometry at the spatial resolution of our data (see Sect. 4.2). The final correction is a multiplicative term that is stored as a 2D image/map in a new HDU (FLAT). The correction can be easily undone by the user by dividing the Primary and the ERROR datacubes by the content of this HDU without altering any of the other properties of the data cubes. This HDU is present only for those galaxies where the SDSSflat correction is applied.

5.5. FITS header information

The FITS header contains the standard keywords that encode the information required to transform the pixel-space coordinates into sky and wavelength-space coordinates, following the WCS. Each CALIFA datacube contains the full FITS header information of all raw frames from which it was created. Information regarding observing and instrumental conditions such as sky brightness, flexure offsets, Galactic extinction or approximate

limiting magnitude is also kept in the FITS header of each datacube. See Sect. 4.3 and Table 4 of Husemann et al. (2013) and Sect. 5.4 of García-Benito et al. (2015) for nomenclature and a summary of the main header keywords and their meaning.

The most important new keyword added in DR3 datacubes is "FLAT_SDSS", which takes a boolean value. It indicates whether or not the SDSS flat correction has been applied in Sect. 4.2. This information is also included in the electronic tables describing the quality of the data.

6. Data quality

The present third and final CALIFA data release (DR3) provides science-ready data for a sample of 646 galaxies observed in the V500 setup, 484 in V1200, and 446 combined "COMBO" cubes. As for the previous data releases, all datacubes have been checked according to a QC protocol. The DR3 QC protocol is similar in many respects to the DR2-QC. However, some modifications were introduced, which are highlighted in this section. The end products of the QC procedure are tables of flags that indicate the quality of the released data products: the observing conditions (denoted by the OBS prefix), the instrumental performance and effectiveness of the data reduction (RED), and the accuracy and quality of the final calibrated data products (CAL). QC assessments are based on measured parameters extracted by the pipeline at different stages of the reduction procedure and on visual checks of spatially-integrated spectra and wavelength-integrated synthetic images.

Each flag can have one of the following values:

- −1 = undefined;
- 0 = good quality – OK;
- 1 = minor issues that do not significantly affect the quality – WARNING;
- 2 = significant issues affecting the quality – BAD.

Flags depending on measured parameters are assigned by checking against thresholds, as detailed below and summarized in Tables 3–5. Below each flag name, in the table we also report the percentage of cubes with OK, WARNING, BAD, and undefined value, in order to provide a quantitative assessment of the impact of each flag on the QC. The thresholds are determined starting from the actual parameter distribution, so as to flag obvious outliers, by comparison with the nominal quality requirements of the survey, and by checking the impact of exceeding such thresholds on the accuracy of the wavelength and spectrophotometric calibration. Visual checks for each datacube are performed by three members of the collaboration. The median of the three independent assessments is taken as the corresponding QC flag. For flags that combine visual classifications and measured parameters, partial flags are created independently and the worst value is retained as the final flag. The tables of QC flags, along with the relevant QC parameters, are available on the DR3 website.

In naming the QC parameters, we adopt the following convention: the first part is the category prefix (OBS, RED or CAL), followed by a measured parameter, and sometimes a final suffix indicating the statistics applied to combine the parameter as measured in different observations/pointings/fibers (i.e., MEAN, MIN, MAX, RMS).

The QC of the V500 and V1200 setups is based on the same set of parameters and visual checks, except for the parameters and flags related to the spectrophotometric comparison with the SDSS (see below and Sect. 6.3), which only applies to the V500 setup. The COMBO cubes inherit all the flags from the corresponding V500 and V1200 "parent" cubes. In addition they are visually inspected to make sure that the combination process did not introduce any defects or artifacts (see Sect. 6.3).

In the following subsections, we describe the QCs in each of the above-mentioned categories. For any practical use, the definition of the flags are summarized in Tables 3–5. Parameters that either are involved in the determination of the QC flags or that can be useful for independent QC assessment by the user are released as "QCpars" tables available on the CALIFA ftp site, along with a short description of the parameters.

6.1. Quality of the observing conditions (OBS)

Three quantities contribute to determine the quality of the observing conditions of the CALIFA data: the airmass, the sky brightness, and the atmospheric extinction. Contrary to DR2, guided by our increased experience, in DR3 observing conditions never raise a BAD flag: in other words, poor observing conditions alone do not imply bad or unsuitable data, but just raise a WARNING.

Note that, as in DR2, we do not consider the seeing in the set of observing condition parameters to set flags, although it is included in the released "QCpars" tables. The reason for this is that, as already pointed out in García-Benito et al. (2015), given the sampling of the fibers on the plane of the sky and the resampling process, the resolution and depth of the CALIFA cubes are largely insensitive to the seeing during the observations.

For the airmass, we consider the average and the maximum airmass of the observations over all contributing pointings (OBS_AIRMASS_MEAN and OBS_AIRMASS_MAX) and its rms (OBS_AIRMASS_RMS). For each of these quantities, we defined a warning threshold, which is more restrictive in V1200 than in V500 due to the more demanding observing conditions for V1200 (see Tables 3 and 4). The combined FLAG_OBS_AM results in a WARNING as long as any of the three quantities exceeds the threshold.

The V-band surface brightness of the sky during the observations (SKYMAG) may limit the depth of the observations and the accuracy of the sky subtraction and therefore contributes in defining the quality of the observing conditions. As for DR2, the quantity SKYMAG is measured in each pointing from the sky spectrum obtained from the 36 sky fibers[4]. The mean and the rms of SKYMAG over all pointings are considered to define the corresponding flags. As for the airmass, stricter requirements are applied to V1200 data than to the V500 data. Note also that the thresholds are different from those adopted in DR2, as a result of our improved understanding of the impact of the sky brightness on our data.

The transparency of the sky during each pointing (EXT) is obtained from the monitored V-band extinction at the time of the observation. Large extinctions on average, a large maximum

---

extinction or a large rms variation across the pointings (indicating inhomogeneous observing conditions) set a WARNING flag, according to the thresholds reported in Tables 3 and 4.

6.2. Quality of the instrumental/data reduction performance (RED)

We assess the quality of the instrumental and data reduction performance based on four different properties as measured on the reduced data *before* combining them into the final datacube: STRAYLIGHT, spectral DISPERSION, cross dispersion CDISP, and the residuals from the subtraction of bright skylines (namely, the 5577 Å O$_2$ line in the V500 setup and the 4358 Å HgI in the V1200 setup). Moreover, we consider the limiting surface brightness corresponding to a 3-σ detection per spaxel and spectral resolution element measured on the final datacube. Additionally we check that the final datacube does not present a pathological fraction of bad pixels, i.e. pixels characterized by large errors (5 times larger than the absolute value of the flux). Thresholds on this fraction RED_FRAC_BIGERR are given in order to raise a WARNING or a BAD FLAG_RED_ERRSPEC flag.

The straylight is an additive contribution to the raw spectra that must be removed in the data reduction process. Although the pipeline takes care of the straylight subtraction (see Appendix A.3 of Husemann et al. 2013), we have found that significant residuals that affect the final quality of the data are left whenever a frame presents high mean levels of straylight (MEANSTRAYLIGHT), as well as high maximum values (MAXSTRAYLIGHT) and large rms (RMSSTRAYLIGHT). Tables 3 and 4 report the thresholds above which a WARNING or a BAD FLAG_RED_STRAYLIGHT flag is set, respectively, for the three quantities in any of the contributing 2D frames (as indicated by the _MAX suffix attached to each quantity). Note that we have modified the thresholds adopted in the DR2 to less strict values, based on the larger statistics now available and our greater experience with the data. Specifically, while the original thresholds were set based on the distributions of the parameters and the corresponding percentiles in order to filter out clear outliers, in this release we have anlayzed the actual correspondence of WARNING and BAD flags to real problems in the cubes, thus realizing that the requirements on the straylight for an acceptable reduction could be relaxed.

The light from each fiber is dispersed in the wavelength direction with a given spectral DISPERSION along a trace with a finite width or cross-dispersion FWHM (CDISP). Significant departures of these two quantities from the nominal target values raise a FLAG_RED_DISP and a FLAG_RED_CDISP flag, respectively. This is done by checking the mean values (RED_DISP_MEAN, RED_CDISP_MEAN), the rms (RED_DISP_RMS, RED_CDISP_RMS), and the maximum values (RED_DISP_MAX, RED_CDISP_MAX) against the thresholds provided in Tables 3 and 4 (see footnote 10 in García-Benito et al. 2015, for more details about these quantities). Again, note that the thresholds have been modified with respect to DR2 in order to optimize the effectiveness of the flags. Specifically, we have relaxed the requirements on the maximum values and rms, which could be strongly affected by a few low-quality spaxels, even if the cube has a generally good quality.

The accuracy of the sky subtraction is quantified by the minimum and the maximum over all pointings of the average (over all fibers) flux residual of a bright skyline within an individual pointing (RED_RES4358_MIN and RED_RES4358_MAX, and RED_RES5577_MIN and RED_RES5577_MAX for the V1200

---

4 See Appendix A.8 of Husemann et al. (2013).

Table 3. Definition of CALIFA DR3 quality control flags for the V500 data.

QC flag	QC parameters involved	WARNING condition(s)	BAD condition(s)	Flag definition
FLAG_OBS_AM	OBS_AIRMASS_MEAN	>2.0	...	Worst of the three parameters
[98.1%, 1.9%, 0.0%, 0.0%]	OBS_AIRMASS_MAX	>2.5	...	
	OBS_AIRMASS_RMS	>0.15	...	
FLAG_OBS_SKYMAG	OBS_SKYMAG_MEAN	<19.5 mag$_V$ arcsec^{-2}	...	Worst of the two parameters
[95.5%, 4.5%, 0.0%, 0.0%]	OBS_SKYMAG_RMS	>0.1	...	
FLAG_OBS_EXT	OBS_EXT_MEAN	>0.30 mag	...	Worst of the three parameters
[65.2%, 4.0%, 0.0%, 30.8%]	OBS_EXT_MAX	>0.35	...	
	OBS_EXT_RMS	>0.10	...	
FLAG_RED_STRAYLIGHT	RED_MEANSTRAYLIGHT_MAX	>50 counts	>100	Worst of the three parameters
[84.2%, 1.7%, 3.9%, 10.2%]	RED_MAXSTRAYLIGHT_MAX	>75	>150	
	RED_RMSSTRAYLIGHT_MAX	>15	>30	
FLAG_RED_DISP	RED_DISP_MEAN	>5.5 Å (FWHM)	>10	Worst of the three parameters
[75.1%, 19.0%, 0.0%, 5.9%]	RED_DISP_MAX	>10.0	...	
	RED_DISP_RMS	>0.5	...	
FLAG_RED_CDISP	RED_CDISP_MEAN	>3.0 pixels (FWHM)	...	Worst of the three parameters
[84.1%, 10.2%, 0.0%, 5.7%]	RED_CDISP_MAX	≥ 4.0	...	
	RED_CDISP_RMS	>0.25	...	
FLAG_RED_SKYLINES	RED_RES5577_MIN	<−0.1 counts	...	Worst of the three parameters
[66.1%, 23.8%, 0.0%, 10.1%]	RED_RES5577_MAX	>0.1	...	
	RED_RMSRES5577_MAX	>1.0	...	
FLAG_RED_LIMSB	RED_LIMSB	<23.0 mag$_{AB}$ arcsec^{-2}	<22.5	
[86.5%, 9.9%, 2.9%, 0.6%]				
FLAG_RED_ERRSPEC	RED_FRAC_BIGERR	>0.4	>0.6	
[98.6%, 0.0%, 1.2%, 0.2%]				
FLAG_CAL_SPECPHOTO	CAL_QFLUX_G	>0.06 dex	>0.097 dex	Worst of the three parameters
[67.6%, 21.8%, 10.5%, 0.0%]		<−0.06 dex	<−0.097 dex	combined with visual checks
	CAL_QFLUX_R	>0.06 dex	>0.097 dex	on the 30″-integrated spectrum:
		<−0.06 dex	<−0.097 dex	spectral shape and comparison
	CAL_QFLUX_RMS	>0.1	>0.2	with SDSS photometry
FLAG_CAL_WL	CAL_RMSVELMEAN	>2.0 km s^{-1}	>5.0	
[92.1%, 7.4%, 0.5%, 0.0%]				
FLAG_CAL_IMGQUAL				Visual checks on
[84.8%, 14.9%, 0.0%, 0.3%]				synthetic broad-band image
FLAG_CAL_SPECQUAL				Visual checks on 30″-aperture
[94.6%, 5.4%, 0.0%, 0.0%]				integrated spectrum
FLAG_CAL_FLATSDSS				Visual checks on SDSSflat map,
[47.1%, 43.8%, 0.3%, 8.8%]				and effective SDSSflat response
				from 30″-aperture integrated
				spectrum
				−1 if SDSSflat not applied
FLAG_CAL_REGISTRATION				Visual checks on synthetic
[52.6%, 23.4%, 0.0%, 24.0%]				broad-band image, SDSS footprint,
				and χ^2 surface plots
				−1 if registration relative
				to SDSS not applied

Notes. Numbers in square brackets provide the percentage of released cubes with OK, WARNING, BAD, and undefined value, respectively.

and the V500 setup, respectively). We also consider the maximum over all pointings of the rms residuals (over all fibers in an individual pointing), RED_RMSRES4358_MAX and RED_RMSRES5577_MAX. Large average residuals (in absolute value) are indications of systematic bias in the sky subtraction, while large rms is a symptom of localized failures or noisy data. In these cases, the FLAG_RED_SKYLINES is set.

The FLAG_RED_LIMSB flag is used to classify the quality of datacubes based on the 3σ continuum flux density detection limit per interpolated 1 arcsec^2-spaxel and spectral resolution element. See Sect. 6.7 for a definition of the wavelength

range used to derive this quantity. Thresholds are provided in AB-magnitudes over the spectral window used for the flux integration and have been tuned slightly with respect to DR2.

6.3. Quality of the calibrated data products (CAL)

This part of the QC deals with the final calibrated datacubes and, although similar in many respects, has been significantly modified with respect to DR2.

A series of checks and flags are common to both the V500 and V1200 setups, namely those concerning the quality of the

Table 4. Definition of CALIFA DR3 quality control flags for the V1200 data.

QC flag	QC parameters involved	WARNING condition(s)	BAD condition(s)	Flag definition
FLAG_OBS_AM	OBS_AIRMASS_MEAN	>1.5	...	Worst of the three parameters
[89.3%, 10.7%, 0.0%, 0.0%]	OBS_AIRMASS_MAX	>2.0	...	
	OBS_AIRMASS_RMS	>0.15	...	
FLAG_OBS_SKYMAG	OBS_SKYMAG_MEAN	<21.5 mag_V arcsec^{-2}	...	Worst of the two parameters
[87.6%, 12.4%, 0.0%, 0.0%]	OBS_SKYMAG_RMS	>0.1	...	
FLAG_OBS_EXT	OBS_EXT_MEAN	>0.30 mag	...	Worst of the three parameters
[61.4%, 1.9%, 0.0%, 36.8%]	OBS_EXT_MAX	>0.35	...	
	OBS_EXT_RMS	>0.10	...	
FLAG_RED_STRAYLIGHT	RED_MEANSTRAYLIGHT_MAX	>15 counts	>30	Worst of the three parameters
[76.9%, 13.4%, 5.6%, 4.1%]	RED_MAXSTRAYLIGHT_MAX	>20	>50	
	RED_RMSSTRAYLIGHT_MAX	>1.5	>3.0	
FLAG_RED_DISP	RED_DISP_MEAN	>2.3 Å (FWHM)	>2.5	Worst of the three parameters
[78.1%, 19.2%, 0.0%, 2.7%]	RED_DISP_MAX	>3.0	...	
	RED_DISP_RMS	>0.2	...	
FLAG_RED_CDISP	RED_CDISP_MEAN	>3.0 pixels (FWHM)	...	
[68.0%, 29.3%, 0.0%, 2.7%]				
FLAG_RED_SKYLINES	RED_RES4358_MIN	<−0.1 counts	...	Worst of the three parameters
[62.6%, 33.3%, 0.0%, 4.1%]	RED_RES4358_MAX	>0.1	...	
	RED_RMSRES4358_MAX	>0.7	...	
FLAG_RED_LIMSB	RED_LIMSB	<22.5 mag_{AB} arcsec^{-2}	<22.0	
[93.8%, 4.3%, 1.9%, 0.0%]				
FLAG_RED_ERRSPEC	RED_FRAC_BIGERR	>0.4	>0.6	
[99.8%, 0.2%, 0.0%, 0.0%]				
FLAG_CAL_WL	CAL_RMSVELMEAN	>1.0 km s^{-1}	>2.0	
[98.1%, 1.7%, 0.0%, 0.2%]				
FLAG_CAL_IMGQUAL				Visual checks on synthetic broad-band image
[88.8%, 9.7%, 0.0%, 1.4%]				
FLAG_CAL_SPECQUAL				Visual checks on 30″-aperture integrated spectrum
[91.9%, 7.6%, 0.0%, 0.4%]				
FLAG_CAL_FLATSDSS				Visual checks on SDSSflat map, and effective SDSSflat response from 30″-aperture integrated spectrum −1 if SDSSflat not applied
[55.6%, 36.0%, 0.0%, 8.5%]				
FLAG_CAL_REGISTRATION				Visual checks on synthetic broad-band image, SDSS footprint, and χ^2 surface plots −1 if registration relative to SDSS not applied
[33.1%, 35.5%, 0.2%, 31.2%]				

Notes. Numbers in square brackets provide the percentage of released cubes with OK, WARNING, BAD, and undefined value, respectively.

synthetic image (FLAG_CAL_IMGQUAL), of the integrated 30″-aperture spectra (FLAG_CAL_SPECQUAL), the wavelength accuracy and stability (FLAG_CAL_WL), and, when applicable, the quality of the "SDSS flat-field" (see below and Sect. 5.4) and of the registration on the plane of sky relative to SDSS imaging (see below and García-Benito et al. 2015). For V500 only, in addition we perform checks on the spectrophotometric accuracy that determine the FLAG_CAL_SPECPHOTO flag. Additional checks are visually performed on the synthetic images and the 30″-aperture spectra for COMBO cubes. Wavelength accuracy and stability (FLAG_CAL_WL) are performed on COMBO cubes as well.

Visual checks on the reconstructed synthetic images in V-band (V500 and COMB) and B-band (V1200 and COMB) are encoded in the FLAG_CAL_IMGQUAL flag and take into account the quality of the images in absolute terms and in comparison to the corresponding g-band SDSS image. Reasons to raise a WARNING or a BAD flag are: holes, artefacts of any kind, irregular

background, ghosts, evident noise patterns, duplicate/offset images of the same sources, significantly elongated PSF. A BAD FLAG_CAL_IMGQUAL flag implies that the datacube is not suitable for any scientific use and occurs whenever multiple images are spotted, indicating a serious problem in the (relative) registration of the pointings, or when a substantial fraction of the image is affected by anomalous background subtraction. Noise patterns or background problems over a limited region are usually flagged as WARNING.

Visual checks on the 30″-aperture spectra are meant to flag anomalies in the overall spectral shape, such as bumps, drops, anomalously low S/N (possibly in limited spectral ranges), and are encoded into the FLAG_CAL_SPECQUAL flag. A BAD classification in this flag implies that the cube is not useful for any science and therefore is not released.

Whenever possible, pipeline V2.2 renormalizes the spectra in each spaxel to match the photometric fluxes derived from the

Table 5. Definition of CALIFA DR3 quality control flags *additional* for the COMB data.

QC flag	QC parameters involved	WARNING condition(s)	BAD condition(s)	Flag definition
FLAG_CAL_IMGQUAL [76.0%, 24.0%, 0.0%, 0.0%]				Visual checks on synthetic broad-band image
FLAG_CAL_SPECQUAL [96.6%, 3.4%, 0.0%, 0.0%]				Visual checks on 30″-aperture integrated spectrum
FLAG_CAL_v1200v500 [79.6%, 20.4%, 0.0%, 0.0%]				Visual checks on the match of the 30″-aperture integrated spectra in V500, V1200 and resulting COMB
FLAG_CAL_WL [97.8%, 2.2%, 0.0%, 0.0%]	CAL_RMSVELMEAN	>2.0 km s^{-1}	>5.0	

Notes. Numbers in square brackets provide the percentage of released cubes with OK, WARNING, BAD, and undefined value, respectively.
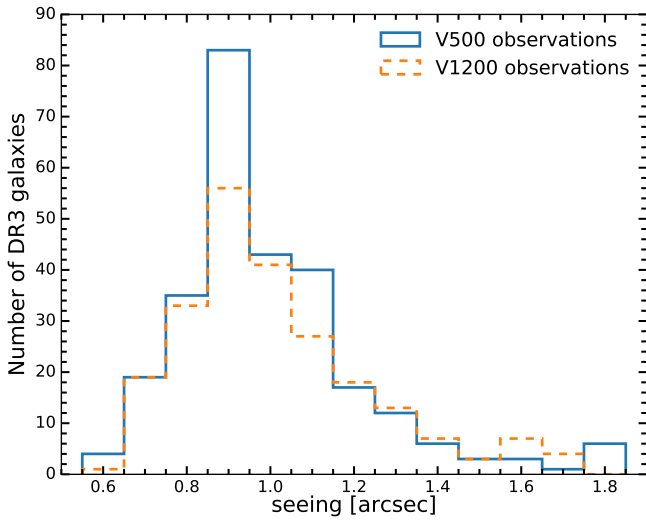
Fig. 8. Distribution of the seeing during the CALIFA observations as measured by the automatic Differential Image Motion Monitor (DIMM, Aceituno 2004).

co-registered SDSS images, by applying the SDSSflat correction. The map of the SDSS flat-fielding function is visually inspected, as well as are the synthetic images and the 30″-aperture integrated spectra before and after applying the SDSSflat. Since the reduced data cubes are already flux-calibrated before applying the SDSSflat, the correction applied in this step must be small, a few percent at most. Large correction factors and/or strong spatial variations, possibly due to bad CALIFA versus SDSS co-registration (spatial offsets or badly matched spatial resolution) and resulting in large differences between the integrated spectra before and after the SDSSflat correction, are initially marked with a BAD FLAG_CAL_FLATSDSS. We have then re-checked all such cases and investigated if the problem is due to an independent failure in the observations/data reduction or if it is due to the SDSSflat itself: in the latter case the datacube is re-reduced without the SDSSflat correction and the FLAG_CAL_FLATSDSS is assigned undefined (−1). There are cases where the problem is judged as not amendable and therefore a BAD FLAG_CAL_FLATSDSS is retained. If the problem is flagged as WARNING the SDSSflat correction is retained.

Pipeline V2.2 by default attempts to register the different pointings relative to the SDSS imaging before combining them. The outcome of the process is checked in the QC protocol by visually inspecting i) the footprints of the real CALIFA fibers and of the simulated fibers on the SDSS images based on the

matched astrometric solution and ii) the χ^2 surfaces that describe the goodness of the match between SDSS and CALIFA as a function of the 2D spatial offsets. These checks result in the FLAG_CAL_REGISTRATION flag. If a BAD condition occurs (i.e. obvious mismatch in the pointings relative to SDSS), the datacube is inspected again and re-reduced with the registration based on relative telescope offsets as in the V1.3 pipeline. Section 4.2 and García-Benito et al. (2015) contain more information about the main differences between the two methods. Should this re-reduction produce acceptable results in terms of image and spectral quality, the FLAG_CAL_REGISTRATION is assigned undefined (−1) and the datacube is released, otherwise the FLAG_CAL_IMGQUAL and/or FLAG_CAL_SPECQUAL flags are assigned BAD and the datacube is rejected.

The QC protocol foresees a posteriori flux calibration checks for the V500 setup only, which determine the flag FLAG_CAL_SPECPHOTO. A first quantitative check relies on the visual inspection of the 30″-integrated spectra, whereby the g- and r-band magnitudes derived from SDSS images integrated over the same area are transformed to flux densities and over-plotted on the CALIFA spectrum: significant offsets between the SDSS points and the spectrum raise the flag. The flag is also raised in case of visual checks revealing anomalous spectral shapes (bumps, drops etc.). Finally and more quantitatively the flux ratios in g- and r-band of the different pointings relative to SDSS are considered: deviations in the mean and/or the rms of the flux ratios over the different pointings by more than given thresholds raise the corresponding flag. The flag FLAG_CAL_SPECPHOTO eventually reports the worst classification extracted from all these checks.

In order to check the stability of the wavelength calibration over the full spectral range we performed the same measurements as in DR1 and DR2, as described in Sect. 5.3 of Husemann et al. (2013; see also García-Benito et al. 2015): for each galaxy and setup, the spectra within 5″ of the center of the galaxy are integrated and the systemic velocity is estimated first for the full spectrum and then for 3 (4) independent spectral ranges in the V1200 (V500) setup. The rms of these values with respect to the systemic velocity from the full spectrum (CAL_RMSVELMEAN) is an estimate of the stability of the wavelength calibration across the wavelength range and is used to set the corresponding quality flag FLAG_CAL_WL.

6.4. Overall quality assessment

The flags described in the previous sections allow any potential user to select samples that are most suitable for her/his science goals, using ad hoc selection criteria. However, we identify a set

of key flags for which a BAD classification implies unusable data in any respect: cubes with a BAD in either FLAG_CAL_IMGQUAL, FLAG_CAL_SPECQUAL, FLAG_CAL_WL or FLAG_RED_DISP are therefore excluded from DR3. The sample of galaxies with a released datacube in either one or both of the V500 and V1200 setups satisfying these criteria has been defined as the CALIFA DR3 in Sect. 2.

If one wishes to be more strict, one could restrict all flags to WARNING at most (value ≤1). Such a selection produces a sample we have called the high-quality sample (HQ sample) in section, containing 332 galaxies. An even more stringent restriction would additionally require perfect quality (0 value) in the key flags (FLAG_CAL_IMGQUAL, FLAG_CAL_SPECQUAL, FLAG_CAL_WL, FLAG_RED_DISP). Such a selection would produce a sample of 124 galaxies with the highest quality data. That sample will be limited in size and therefore of less scientific use, but could still be used as a reference sample for making sure that no data imperfections affect scientific conclusions derived from a specific method or paper.

6.5. Seeing and spatial resolution

The average atmospheric seeing conditions during the CALIFA observations were derived from the measurements acquired by the Differential Image Motion Monitor (DIMM, Aceituno 2004), which operates fully automatically at the Calar Alto observatory during the night. The DIMM has different operational constraints from the 3.5 m telescope (humidity lower than 80% and wind speed less than $12 \, \mathrm{m \, s^{-1}}$). Seeing information is thus not available for every CALIFA observation, but the overall seeing distribution is not expected to be very different (see footnote 12 of García-Benito et al. 2015).

Figure 8 shows the DIMM seeing distribution for the DR3 sample, which has a median value of 1″0 FWHM, and therefore atmospheric seeing is not a limiting factor in the spatial resolution of the CALIFA cubes. Therefore, the final spatial resolution of the CALIFA data is mainly set by fiber size and the dithering and interpolation scheme.

We used the following approach to measure the PSF in the datacubes. Since January 2012 standard stars were observed using the same dithering pattern adopted for the science observations for both setups. Only a fraction of the nights had weather conditions good enough to acquire a calibration star using this scheme, yielding a total of 182 stars observed using the dithering scheme. We reduced these data using the same procedure described before for the science objects. The PSF can be measured very precisely because the calibration stars have a very high S/N. We took images based on slices of width 400 Å in wavelength from the datacubes for each of these stars. For each of these images, we fitted a 2D Moffat profile (see Eq. (1)) using the software IMFIT (Erwin 2015). Figure 9 shows the normalized distributions of FWHM and β_M parameters of the Moffat profile, weighted by the likelihood of the fit, for all wavelengths and all stars. Counts are normalized to form a probability density so the integral of the histogram is 1. The fits do not show any significant wavelength dependence in any of those parameters. We obtained a mean value and 1σ scatter of the FWHM as 2.50 ± 0.34 arcsec. The distribution of β_M is asymmetric, so a better estimate of its value is the weighted median, which gives $\beta_M = 2.15$. The ellipticity ($1 - b/a$, with a and b being the semimajor and semiminor axes, respectively) is also measured, with mean value and 1σ scatter of 0.08 ± 0.06. Given the uncertainties, this value means the PSF can be considered effectively
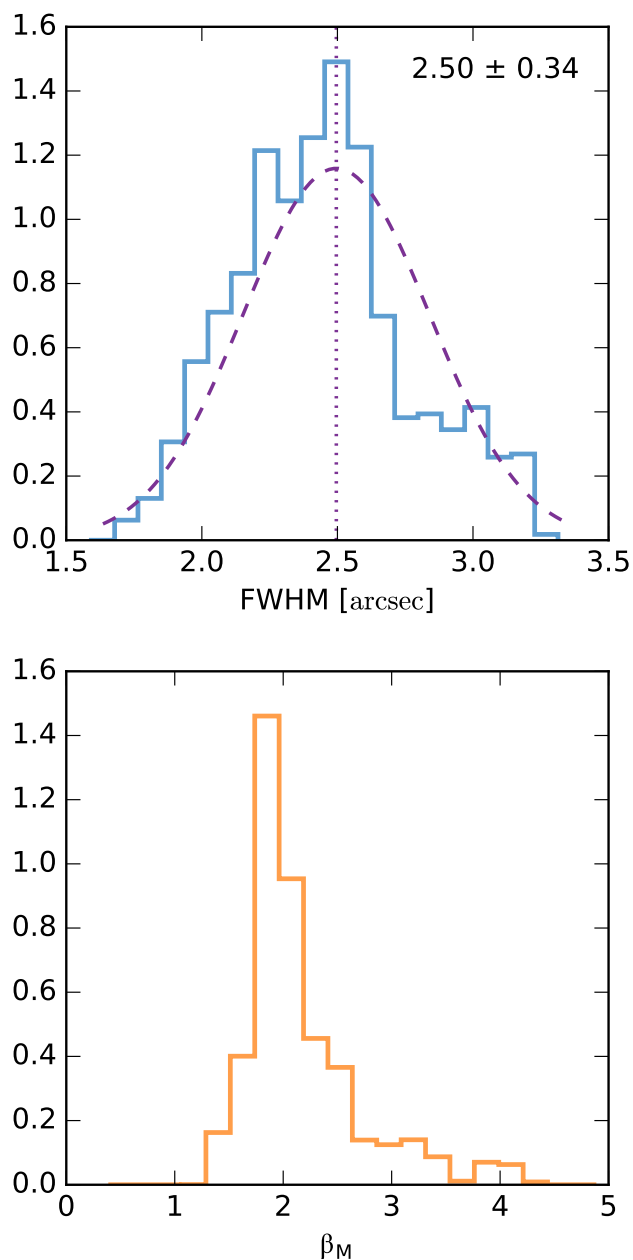
Fig. 9. Normalized distributions of the integrated area of the PSF FWHM (*top panel*) and β_M (*bottom panel*) parameters of an elliptical 2D Moffat profile fitted to 63 calibration stars, weighted by the likelihood of the fit. In the *top panel* the normal probability density function is marked with a dashed line and the dotted line indicates the mean value of the distribution.

axisymmetric. The uncertainties in these measurements correspond to 1σ of the distributions. Note that the distribution is broader than that reported for DR2 (García-Benito et al. 2015) because in that release we discarded galaxies observed under observing conditions with high seeing.

6.6. Spectrophotometric accuracy

As described in Sect. 4.1 the registration scheme of the pipeline rescales the datacubes to the absolute flux level of the SDSS DR7 broad-band photometry, using the *r*-band image for the V500
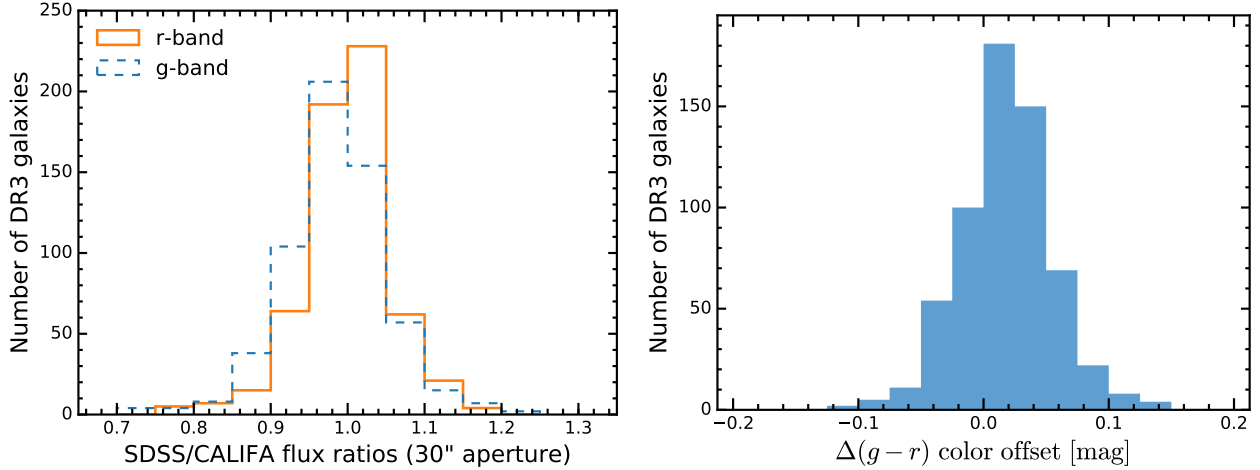
Fig. 10. *Left panel*: distribution of the 30″ aperture photometry scale factor between the SDSS DR7 images and recalibrated CALIFA data. We compare the photometry only for the *g*- and *r*-bands, which are both entirely covered by the V500 wavelength range. *Right panel*: distribution of the corresponding color offset between the SDSS DR7 images and the synthetic CALIFA broadband images.

setup and the *g*-band image for the V1200 setup. On the other hand, for the COMBO cubes the V1200 data are finally matched to the V500 data. These procedures, together with the recalibrated sensitivity curve (see Sect. 4.2), and the updated calibration frames (master skyflats, master bias...) improves the spectrophotometric calibration of DR3 relative to DR1 and DR2.

This is clearly shown in Fig. 10. As part of the CALIFA pipeline V2.2, a 30″ diameter photometric aperture in *r* and *g* is measured both in the SDSS DR7 images and in the equivalent synthetic CALIFA broadband images. The mean SDSS/CALIFA *g*- and *r*-band ratios in DR3 and their scatter are 0.99 ± 0.09 and 1.00 ± 0.08, respectively. In the *right panel* of Fig. 10 the distribution in $\Delta(g - r)$ color difference between the SDSS and CALIFA data shows that the spectrophotometric accuracy over the wavelength range is better than 4%, with a median value of 0.02 ± 0.04.

We use spectral fitting methods to make an independent estimate of the spectrophotometric accuracy, following Husemann et al. (2013) and García-Benito et al. (2015). We repeat a similar experiment for the DR3 datacubes, but in this case we use the results from the fitting performed by Pipe3D (Sánchez et al. 2016). Results are shown in Fig. 11. The top panel shows in blue the mean spectrum of 251313 spatial bins of 446 galaxies included in the DR3 COMBO distribution with $S/N > 15$ in the continuum at ~5635 Å and good quality spectral fitting. The average is taken after normalizing each spectrum by its median flux in the 5635 ± 45 Å window. The mean synthetic spectrum (overplotted orange line) as well as the mean residual (at the bottom of the upper panel, purple line) are also plotted. The bottom panel zooms in on the residual spectrum.

The layout of Fig. 11 is similar to Fig. 13 in Cid Fernandes et al. (2014) or Fig. 18 in García-Benito et al. (2015), to which it should be compared. Focusing on the middle panel, one sees that from ~5000 Å to the red the residuals are very similar, including the humps around 5800 Å associated with the imperfect removal of telluric features. Toward the blue however, the reduction pipeline leads to smaller residuals than that of version V1.3c, with characteristics very similar to those of version V1.5.

In addition to the previous test, we also performed an independent estimation of the accuracy of the spectrophotometric calibration by comparing the flux-calibrated spectra of the stars observed using the three dithering procedures (Sect. 6.5) with

their published spectra. Since all those stars are spectrophotometric standards, they have high-S/N and good quality published spectra.

We performed the same spectrophotometric calibration for these stars than the one applied to the science cubes, using the same sensitivity curve and atmospheric extinction (Sect. 4.2). Then we extracted a 30″ aperture spectrum over the DAR-corrected datacube corresponding to each calibration star. Finally we compared those spectra with the published ones, deriving a ratio of 0.99 ± 0.10, as can be seen in Fig. 12. Thus, the absolute spectrophotometric accuracy is around ~10%, a result that was anticipated by García-Benito et al. (2015). This was the reason why we decided not to use the calibration stars to derive the sensitivity curve. Once corrected for the absolute spectrophotometric offset, the average spectra derived for each calibration star agree with the published ones within ~3.4% from blue to red. Figure 13 shows the comparison between the derived spectrum of the spectrophotometric standard star Hz44 and the published one (Oke 1990), showing a high degree of agreement.

6.7. Limiting sensitivity and signal-to-noise

To assess the depth of the data, we estimate the 3σ continuum flux density detection limit per interpolated 1 arcsec²-spaxel and spectral resolution element for the faintest regions. Figure 14 shows the limiting continuum sensitivity of the spectrophotometrically recalibrated CALIFA cubes. The depth is plotted against the average S/N per 1 arcsec² and spectral resolution element within an elliptical annulus of ±1″ around the galaxies' *r*-band half-light semimajor axis (HLR), with position angle (PA) and radius values taken from Walcher et al. (2014) when available or directly from the datacube. A narrow wavelength window at 4480–4520 Å for the V1200 and at 5590–5680 Å for the V500 is used to estimate both values. Specifically, the signal (also used for the surface brightness limit) is computed as the median value in the defined wavelength intervals, while the noise is the detrended standard deviation in the same windows. These small windows are nearly free of stellar absorption features or emission lines. The 3σ continuum flux density detection limit per spaxel and spectral resolution element[5] for the V1200

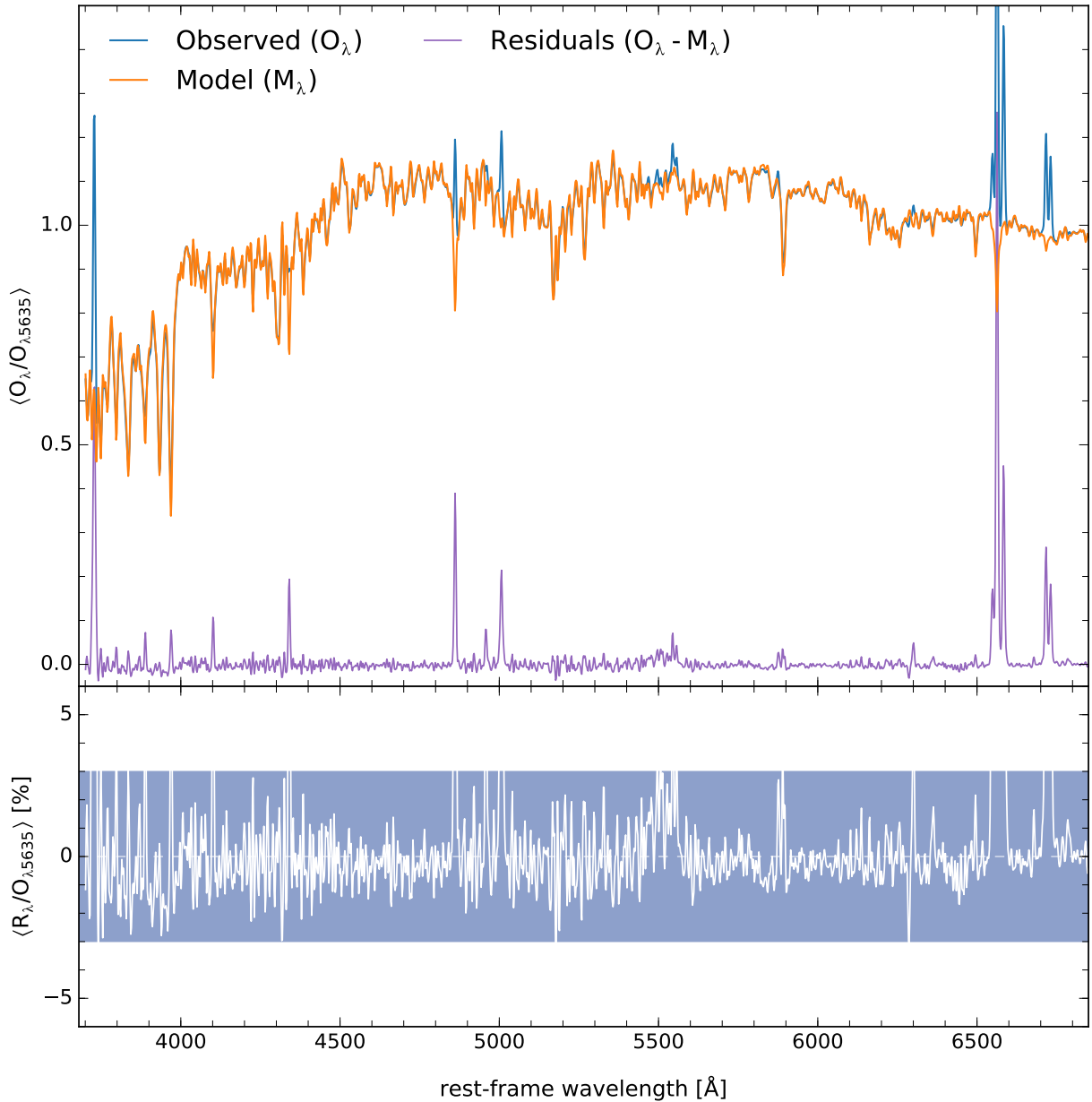[5] We note that this is a continuum flux density. See Note 5 of Husemann et al. (2013).

Fig. 11. Statistics of the spectral residuals. *Top panel*: the mean normalized spectrum of 251313 bins from 446 galaxies. The mean Pipe3D fit is overplotted in orange, while the mean residual is plotted at the bottom of the panel (purple). *Bottom panel*: zoom of the residual spectrum. The shaded rectangle encompasses the ±3% area.

data ($I_{3\sigma} = 3.0 \times 10^{-18}$ erg s^{-1} cm^{-2} Å^{-1} arcsec^{-2} in the median at 4500 Å) is a factor of ~2–3 brighter than for the V500 data ($I_{3\sigma} = 1.3 \times 10^{-18}$ erg s^{-1} cm^{-2} Å^{-1} arcsec^{-2} in the median at 5635 Å) mainly because of the difference in spectral resolution. These continuum sensitivities can be transformed into equivalent limiting broadband surface brightnesses of 23.0 mag arcsec^{-2} in the g-band for the V1200 data and 23.4 mag arcsec^{-2} in the r-band for the V500 data. The variance of the sky brightness on each night might be one of the main factors causing the difference in the limiting continuum sensitivity. Dust attenuation, transparency of the night, and other atmospheric conditions might also affect the depth achievable at fixed exposure times.

The limiting sensitivity is also a measure of the noise due to observing conditions and thus it correlates mildly with the S/N at one HLR. The mean S/N in the continuum per 1 arcsec^2 and

spectral resolution element at the HLR along the semimajor axis for all objects is ~9.4 for the V1200 setup, while it is ~21.2 for the V500 setup. Thus, we achieve a $S/N \gtrsim 10$ at 1 HLR for a significant number of the objects for the V500 setup (~85%) and even for the V1200 setup (~40%).

7. Access to the CALIFA DR3 data

7.1. The CALIFA DR3 search and retrieval tool

The public data are distributed through the CALIFA DR3 web page[6]. A simple web form interface, already in use for DR1 and DR2, allows the user to select data of a particular target galaxy,

---

[6] http://califa.caha.es/DR3
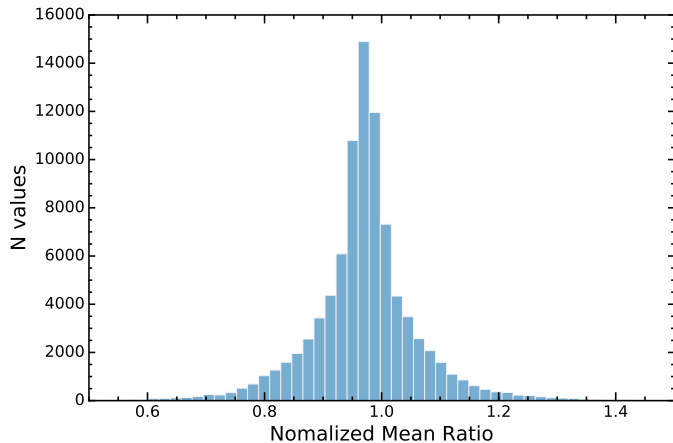
Fig. 12. Histogram of the differences between flux intensities for the published spectra for the spectrophotometric calibration stars described in Sect. 6.5 and the corresponding ones derived by CALIFA.
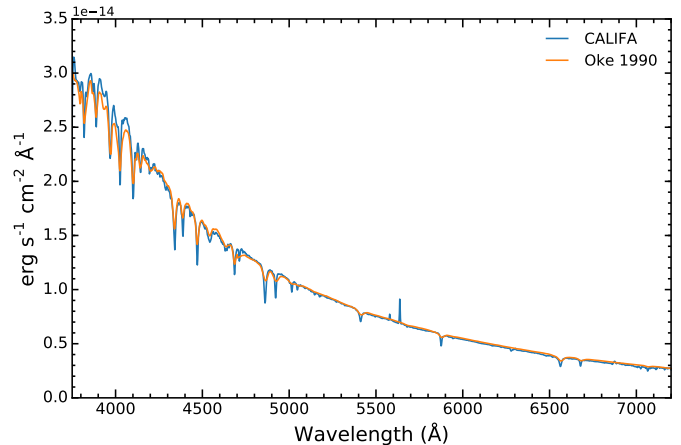

Fig. 13. Comparison between the published spectrum for the spectrophotometric standard star Hz44 and the average of the 15 spectra derived by CALIFA for the same star.

or a sub-sample of objects within some constraints on observing conditions or galaxy properties. Among the selection parameters, we include the instrument setup, galaxy name and coordinates, redshift, g-band magnitudes, Hubble type, bar strength and whether or not it is a clearly merging system.

If any CALIFA datasets are available given the search parameters, they are listed in the search results and can be selected for download. The download process requests a target directory on the local machine to store the data, after the downloading option is selected. The CALIFA data are delivered as fully reduced datacubes in FITS format separately for each of the three configurations: V500, V1200 and COMBO. Each DR3 datacube is uniquely identified by its file name, *GALNAME*.`V1200.rscube.fits.gz`, *GALNAME*.`V500.rscube.fits.gz` and *GALNAME*.`COMB.rscube.fits.gz` for the V1200, V500 and COMBO configurations respectively, where *GALNAME* is the CALIFA ID number listed in the electronically distributed tables.

All the QC tables discussed throughout this article are also distributed in CSV and FITS-table formats on the DR3 webpage. In addition, we distribute the tables discussed in Walcher et al. (2014) and in Sect. 2 regarding the characterization of the Main and extension samples, using similar formats. These tables could be useful for further science exploitation of the datacubes.

7.2. Virtual observatory services

Just like the previous data releases, the CALIFA DR3 also interfaces with Virtual Observatory (VO) facilities. At release time or shortly thereafter, the datacubes will be made available through the Obscore data model, and as database tables of voxels in the TAP service `ivo://org.gavo.dc/tap`[7]. The service also contains tables of objects and QC parameters. These and further services can also be found by searching for CALIFA DR3 with any registry client.

8. Summary

In this article we have presented the main characteristics of the Third public data release, DR3, of the Calar Alto Legacy Integral Field Area (CALIFA) survey. DR3 comprises 667 galaxies (1576 datacubes) containing information from more than 1.5 million independent spectra, covering a wide range of masses, morphological types, and colors. The released datacubes correspond to two different sample of galaxies: i) the main sample, a randomly selected subsample of the CALIFA mother sample comprising 529 galaxies and representative of galaxies in the local Universe and ii) an Extension Sample comprising a heterogeneous collection of galaxies observed with the same setup that adds objects that are rare in the overall galaxy population and therefore not numerous or absent in the mother sample. The CALIFA DR3 provides science-grade and quality-checked integral-field spectroscopic data to the community[8].

We reduced the data using a new version of the pipeline (V2.2), which slightly improves the quality of the data in terms of: i) reliability of the spatial registration process; ii) the homogeneity in the data reduction; and iii) the quality of the image reconstruction. We described in detail the main quality parameters analyzed in the validation process, which are provided to users with complete tables to select the most suitable objects for their science cases.

Compared with other ongoing major surveys, CALIFA offers a similar projected spatial resolution. The PSF of the datacubes has a mean value of ~2.5″ (Sect. 6.5), similar to those reported SAMI (Sharp et al. 2015) and MaNGA (Law et al., in prep.). However, CALIFA galaxies are observed at lower redshift and with a physically larger IFU, thus providing better spatial coverage and resolution, as well as better overall S/N. CALIFA thus offers a highly competitive compromise for analyzing the spatially resolved structures in galaxies. The penalty for this wider coverage is the lower number of galaxies observed (6 times lower than what is projected for SAMI and 15 times lower than the goals of MaNGA), and a lower spectral resolution over the full wavelength range.

While the CALIFA data distributed in this final DR have already been used for a variety of science applications, the potential for new scientific exploitation of the data is still very high. As CALIFA has been conceived as a legacy survey, we sincerely hope that the data will be useful to the community in years to come.
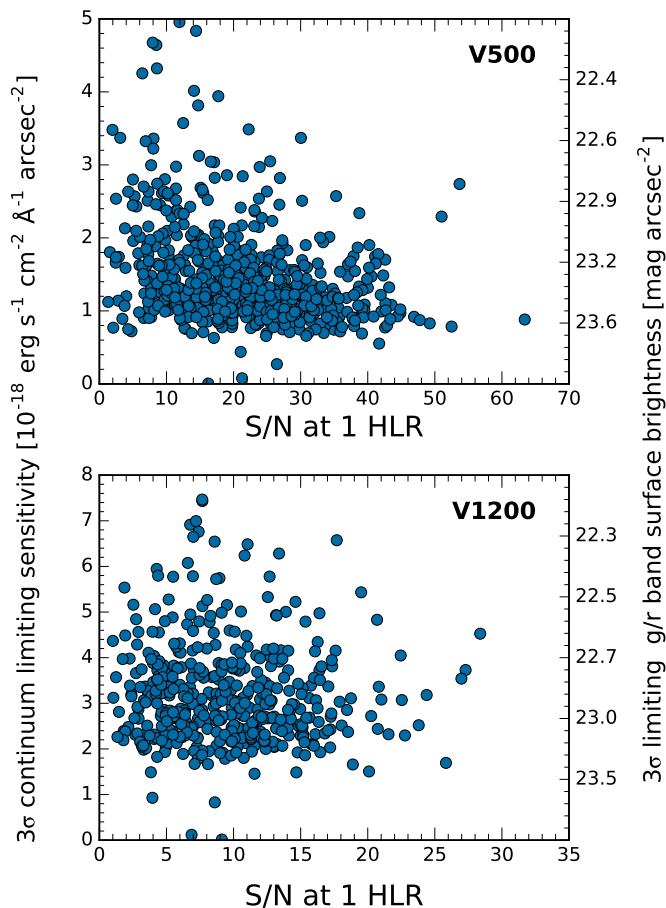
---

7   Accessible at `http://dc.g-vo.org/tap`

8   `http://califa.caha.es/DR3`

Fig. 14. Limiting 3σ continuum sensitivity per spaxel and spectral resolution element as a function of the average continuum S/N at the half-light radius (HLR). The corresponding broadband surface brightness limits in r (V500) and g (V1200) are indicated on the right y-axis. The limiting continuum sensitivity and the S/N were computed from the median signal and noise in the wavelength region 4480–4520 Å and 5590–5680 Å for the V1200 and V500 data, respectively.

References

Aceituno, J. 2004, Calar Alto Newsletter No. 8, http://www.caha.es/newsletter/news04b/Aceituno/Newsletter.html
Aguerri, J. A. L., Méndez-Abreu, J., Falcón-Barroso, J., et al. 2015, A&A, 576, A102
Barbon, R., Buondí, V., Cappellaro, E., & Turatto, M. 1999, A&AS, 139, 531
Barrera-Ballesteros, J. K., Falcón-Barroso, J., García-Lorenzo, B., et al. 2014, A&A, 568, A70
Barrera-Ballesteros, J. K., García-Lorenzo, B., Falcón-Barroso, J., et al. 2015a, A&A, 582, A21
Barrera-Ballesteros, J. K., Sánchez, S. F., García-Lorenzo, B., et al. 2015b, A&A, 579, A45
Bershady, M. A., Verheijen, M. A. W., Swaters, R. A., et al. 2010, ApJ, 716, 198
Blanton, M. R., Schlegel, D. J., Strauss, M. A., et al. 2005, AJ, 129, 2562
Bryant, J. J., Owers, M. S., Robotham, A. S. G., et al. 2015, MNRAS, 447, 2857
Bundy, K., Bershady, M. A., Law, D. R., et al. 2015, ApJ, 798, 7
Cano-Díaz, M., Sánchez, S. F., Zibetti, S., et al. 2016, ApJ, 821, L26
Cappellari, M., & Copin, Y. 2003, MNRAS, 342, 345
Cappellari, M., Emsellem, E., Krajnović, D., et al. 2011, MNRAS, 413, 813
Cardelli, J. A., Clayton, G. C., & Mathis, J. S. 1989, ApJ, 345, 245
Catalán-Torrecilla, C., Gil de Paz, A., Castillo-Morales, A., et al. 2015, A&A, 584, A87
Chabrier, G. 2003, PASP, 115, 763
Cid Fernandes, R., Pérez, E., García Benito, R., et al. 2013, A&A, 557, A86
Cid Fernandes, R., González Delgado, R. M., García Benito, R., et al. 2014, A&A, 561, A130
Croom, S. M., Lawrence, J. S., Bland-Hawthorn, J., et al. 2012, MNRAS, 421, 872
Davies, R. L., Kewley, L. J., Ho, I.-T., & Dopita, M. A. 2014, MNRAS, 444, 3961
De Geyter, G., Baes, M., Camps, P., et al. 2014, MNRAS, 441, 869
Driver, S. P., Norberg, P., Baldry, I. K., et al. 2009, Astron. Geophys., 50, 5.12
Erwin, P. 2015, ApJ, 799, 226
Falcón-Barroso, J., Lyubenova, M., & van de Ven, G. 2015, in IAU Symp. 311, eds. M. Cappellari, & S. Courteau, 78
Galbany, L., Stanishev, V., Mourão, A. M., et al. 2014, A&A, 572, A38
Galbany, L., Stanishev, V., Mourão, A. M., et al. 2016, A&A, 591, A48
García-Benito, R., Zibetti, S., Sánchez, S. F., et al. 2015, A&A, 576, A135
García-Lorenzo, B., Márquez, I., Barrera-Ballesteros, J. K., et al. 2015, A&A, 573, A59
Gomes, J. M., Papaderos, P., Kehrig, C., et al. 2016, A&A, 588, A68
González Delgado, R. M., Cid Fernandes, R., García-Benito, R., et al. 2014a, ApJ, 791, L16
González Delgado, R. M., Pérez, E., Cid Fernandes, R., & et al. 2014b, A&A, 562, A47
González Delgado, R. M., García-Benito, R., Pérez, E., et al. 2015, A&A, 581, A103
González Delgado, R. M., Cid Fernandes, R., Pérez, E., et al. 2016, A&A, 590, A44
Greisen, E. W., & Calabretta, M. R. 2002, A&A, 395, 1061
Haines, T., McIntosh, D. H., Sánchez, S. F., Tremonti, C., & Rudnick, G. 2015, MNRAS, 451, 433
Ho, I.-T., Kudritzki, R.-P., Kewley, L. J., et al. 2015, MNRAS, 448, 2030
Holmes, L., Spekkens, K., Sánchez, S. F., et al. 2015, MNRAS, 451, 4397
Holwerda, B. W., & Keel, W. C. 2013, A&A, 556, A42
Horne, K. 1986, PASP, 98, 609
Hubble, E. 1936, ApJ, 84, 517
Hubble, E. P. 1926, ApJ, 63

Husemann, B., Kamann, S., Sandin, C., et al. 2012, A&A, 545, A137
Husemann, B., Jahnke, K., Sánchez, S. F., et al. 2013, A&A, 549, A87
Ibarra-Mendel, H. J., Sánchez, S. F., Avila-Reese, V., et al. 2016, MNRAS, accepted [arXiv:1609.01304]
Iglesias-Páramo, J., Vílchez, J. M., Galbany, L., et al. 2013, A&A, 553, L7
Iglesias-Páramo, J., Vílchez, J. M., Rosales-Ortega, F. F., et al. 2016, ApJ, 826, 71
Kalinova, V., Colombo, D., Rosolowsky, E., et al. 2015, MNRAS, submitted [arXiv:1509.03352]
Kehrig, C., Monreal-Ibero, A., Papaderos, P., et al. 2012, A&A, 540, A11
Kelz, A., Verheijen, M. A. W., Roth, M. M., et al. 2006, PASP, 118, 129
López Fernández, R., Cid Fernandes, R., González Delgado, R. M., et al. 2016, MNRAS, 458, 184
Lyubenova, M., Martín-Navarro, I., van de Ven, G., et al. 2016, MNRAS, submitted [arXiv:1606.07448]
Marino, R. A., Rosales-Ortega, F. F., Sánchez, S. F., et al. 2013, A&A, 559, A114
Marino, R. A., Gil de Paz, A., Sánchez, S. F., et al. 2016, A&A, 585, A47
Mármol-Queraltó, E., Sánchez, S. F., Marino, R. A., et al. 2011, A&A, 534, A8
Martín-Navarro, I., Vazdekis, A., La Barbera, F., et al. 2015, ApJ, 806, L31
Martínez-García, E. E., Puerari, I., Rosales-Ortega, F. F., et al. 2014, ApJ, 793, L19
Mast, D., Rosales-Ortega, F. F., Sánchez, S. F., et al. 2014, A&A, 561, A129
Oke, J. B. 1990, AJ, 99, 1621
Pagel, B. E. J., & Edmunds, M. G. 1981, ARA&A, 19, 77
Papaderos, P., Gomes, J. M., Vílchez, J. M., et al. 2013, A&A, 555, L1
Peletier, R. F. 1989, Ph.D. Thesis, University of Groningen, The Netherlands
Pérez, E., Cid Fernandes, R., González Delgado, R. M., et al. 2013, ApJ, 764, L1
Roche, N., Humphrey, A., Gomes, J. M., et al. 2015, MNRAS, 453, 2349
Roth, M. M., Kelz, A., Fechner, T., et al. 2005, PASP, 117, 620
Ruiz-Lara, T., Pérez, I., Florido, E., et al. 2016, MNRAS, 456, L35
Sánchez, S., Sánchez-Menguiano, L., Marino, R., et al. 2015, Galaxies, 3, 164
Sánchez, S. F. 2006, Astron. Nachr., 327, 850
Sánchez, S. F. 2015, in Galaxies in 3D across the Universe, eds. B. L. Ziegler, F. Combes, H. Dannerbauer, & M. Verdugo, IAU Symp., 309, 85
Sánchez, S. F., Cardiel, N., Verheijen, M. A. W., Pedraz, S., & Covone, G. 2007, MNRAS, 376, 125
Sánchez, S. F., Kennicutt, R. C., Gil de Paz, A., et al. 2012a, A&A, 538, A8 (S12)
Sánchez, S. F., Rosales-Ortega, F. F., Marino, R. A., et al. 2012b, A&A, 546, A2
Sánchez, S. F., Rosales-Ortega, F. F., Jungwiert, B., et al. 2013, A&A, 554, A58
Sánchez, S. F., Rosales-Ortega, F. F., Iglesias-Páramo, J., et al. 2014, A&A, 563, A49
Sánchez, S. F., Pérez, E., Sánchez-Blázquez, P., et al. 2016, Rev. Mex. Astron. Astrofis., 52, 171
Sánchez-Blázquez, P., Rosales-Ortega, F. F., Méndez-Abreu, J., et al. 2014, A&A, 570, A6
Sánchez-Menguiano, L., Sánchez, S. F., Pérez, I., et al. 2016, A&A, 587, A70
Schlegel, D. J., Finkbeiner, D. P., & Davis, M. 1998, ApJ, 500, 525
Schmidt, M. 1968, ApJ, 151, 393
Sharp, R., Allen, J. T., Fogarty, L. M. R., et al. 2015, MNRAS, 446, 1551
Singh, R., van de Ven, G., Jahnke, K., Lyubenova, M., & et al. 2013, A&A, 558, A43
van den Bosch, R. C. E., Gebhardt, K., Gültekin, K., Yıldırım, A., & Walsh, J. L. 2015, ApJS, 218, 10
Verheijen, M. A. W., Bershady, M. A., Andersen, D. R., et al. 2004, Astron. Nachr., 325, 151
Walcher, C. J., Wisotzki, L., Bekeraité, S., et al. 2014, A&A, 569, A1 (W14)
Wild, V., Rosales-Ortega, F., Falcón-Barroso, J., et al. 2014, A&A, 567, A132
Yıldırım, A., van den Bosch, R. C. E., van de Ven, G., et al. 2016, MNRAS, 456, 538
Yıldırım, A., van den Bosch, R. C. E., van de Ven, G., et al. 2015, MNRAS, 452, 1792
York, D. G., Adelman, J., Anderson, Jr., J. E., et al. 2000, AJ, 120, 1579

[1] Instituto de Astronomía, Universidad Nacional Autonóma de México, A.P. 70-264, 04510, México, D.F.
e-mail: sfsanchez@astro.unam.mx
[2] Instituto de Astrofísica de Andalucía (IAA/CSIC), Glorieta de la Astronomía s/n Aptdo. 3004, 18080 Granada, Spain,
[3] INAF-Osservatorio Astrofisico di Arcetri – Largo Enrico Fermi, 5, 50125 Firenze, Italy
[4] Leibniz-Institut für Astrophysik Potsdam (AIP), An der Sternwarte 16, 14482 Potsdam, Germany
[5] European Southern Observatory, Karl-Schwarzschild-Str. 2, 85748 Garching b. München, Germany
[6] Millennium Institute of Astrophysics, Universidad de Chile, Santiago, Chile
[7] Departamento de Astronomía, Universidad de Chile, Casilla 36-D, Santiago, Chile
[8] Instituto de Astrofísica de Canarias, Vía Láctea s/n, 38205 La Laguna, Tenerife, Spain
[9] University of Vienna, Department of Astrophysics, Türkenschanzstr. 17, 1180 Vienna, Austria
[10] Departamento de Astrofísica, Universidad de La Laguna, 38205 La Laguna, Tenerife, Spain
[11] Observatorio Astronómico, Laprida 854, X5000BGR, Córdoba, Argentina
[12] Consejo de Investigaciones Científicas y Técnicas de la República Argentina, Avda. Rivadavia 1917, C1033AAJ CABA, Argentina
[13] Centro Astronómico Hispano Alemán de Calar Alto (CSIC-MPG), C/ Jesús Durbán Remón 2–2, 4004 Almería, Spain
[14] Departamento de Física, Universidade Federal de Santa Catarina, PO Box 476, 88040-900 Florianópolis, SC, Brazil
[15] Centro de Astrobiología (CSIC-INTA), Depto. Astrofísica, ESAC Campus, 28691 Villanueva de la Cañada, Madrid, Spain
[16] Department of Physics & Astronomy, Johns Hopkins University, Bloomberg Center, 3400 N. Charles St., Baltimore, MD 21218, USA
[17] Sydney Institute for Astronomy, School of Physics, University of Sydney, NSW 2006, Australia
[18] Instituto de Física e Química, Universidade Federal de Itajubá, Av. BPS, 1303, 37500-903 Itajubá-MG, Brazil
[19] Universität Heidelberg, Zentrum für Astronomie, Astronomisches Rechen-Institut, Mönchhofstraße 12–14, 69120 Heidelberg, Germany
[20] Departamento de Física Teórica, Facultad de Ciencias, Universidad Autónoma de Madrid, 28049 Madrid, Spain
[21] Astronomisches Institut, Ruhr-Universität Bochum, Universitätsstr. 150, 44801 Bochum, Germany
[22] School of Physics and Astronomy, University of St. Andrews, SUPA, North Haugh, KY16 9SS, St. Andrews, UK
[23] Departamento de Física Teórica y del Cosmos, University of Granada, Facultad de Ciencias (Edificio Mecenas), 18071 Granada, Spain
[24] Departamento de Astrofísica y CC. de la Atmósfera, Universidad Complutense de Madrid, 28040 Madrid, Spain
[25] Department of Physics, Royal Military College of Canada, PO box 17000, Station Forces, Kingston, Ontario, Canada, K7K 7B4
[26] Institute of Astronomy, University of Cambridge, Madingley Road, Cambridge CB3 0HA, UK
[27] Kapteyn Astronomical Institute, University of Groningen, Postbus 800, 9700 AV Groningen, The Netherlands
[28] Institut für Astronomie (ETH), Wolfgang-Pauli-Str. 27, 8093 Zürich, Switzerland
[29] CIEMAT, Avda. Complutense 40, 28040 Madrid, Spain
[30] GEPI, Observatoire de Paris, CNRS, Université Paris Diderot, Place Jules Janssen, 92190 Meudon, France
[31] Observatorio do Valongo, Universidade Federal do Rio de Janeiro, Ladeira do Pedro Antônio 43, Saúde, 20080-090 Rio de Janeiro, Brazil
[32] Departamento de Astronomía, Universidad de Guanajuato, Apartado Postal 144, 36000 Guanajuato, Guanajuato, Mexico
[33] Instituto Nacional de Astrofísica, Óptica y Electrónica, Luis E. Erro 1, 72840 Tonantzintla, Puebla, Mexico
[34] Instituto de Astrofíisica, Pontificia Universidad Católica de Chile, Av. Vicuña Mackenna 4860, 782-0436 Macul, Santiago, Chile
[35] Max-Planck-Institut für Astronomie, Königstuhl 17, 69117 Heidelberg, Germany